Private 5G Networks for Connected Industries

Deliverable D3.1

Report on Measurements & Network Planning Methodology

Co-funded by the Horizon 2020 programme
of the European Union in collaboration with Taiwan

Date of Delivery: 02.08.2021
Project Start Date: 01.10.2019 **Duration:** 36 Months

Document Information

Project Number:	861459
Project Name:	Private 5G Networks for Connected Industries

Document Number:	D3.1
Document Title:	Report on Measurements & Network Planning Methodology
Editor:	Sergio Barbarossa (SAP)
Authors:	Mathis Schmieder (HHI), Sven Wittig (HHI), Alper Schultze (HHI), Jack Shi-Jie Luo (ITRI), Frank Li-Fong Lin (ITRI), Henrik Klessig (BOSCH), Stefania Sardellitti (SAP), Jiun-Cheng Huang, Cheng-Yi Chien, Yueh-Feng Li, Ling-Chih Kao (CHT), CC Weng (ANI)
Dissemination Level:	Public
Contractual Date of Delivery:	31/07/2021
Work Package	WP3
File Name:	861459-5G_CONNI-D3.1_Report_on_Measurements_Network_Planning_Methodology-v4.0.docx

Revision History

Version	Date	Comment
0.1	20.01.2021	First Skeleton
0.2	24.03.2021	State of the art
3.2	16.07.2021	Version sent to external review for feedback
3.3	29.07.2021	Final version
3.4	16.05.2022	Addressed issues in request for revision
3.5	19.12.2022	Revisited K-Factor; Added comparison between IMTC simulation and model data based on measurements at Bosch site
3.6	19.12.2022	Editorial changes
4.0	19.12.2022	Revised version for submission

Executive Summary

The scope of this deliverable is to report the results of the research carried out within WP3, including the results of the measurement campaigns and the corresponding channel modelling analysis, conducted within Task 3.1, and providing information on the advancements in the developments in application-specific network planning methodology and tools, as part of the activities conducted in Task 3.2. In spite of the very critical circumstances due to the restrictions associated to the spread of the Covid-19 pandemic, that created severe difficulties in accessing the Bosch's premises to carry out the measurement campaign, finally, the measurements have been conducted and this deliverable reports some very interesting results in terms of channel modelling, as derived from the measurement campaign.

List of Figures

List of Acronyms

5G CONNI	5G for Connected Industries
APDP	Average power delay profile
BLER	Block Error Ratio
CDF	Cumulative distribution function
CIR	Channel impulse response
CNC	Computer Numerical Control
CQI	Channel Quality Indicator
CSI	Channel state information
CSI-RS	Channel State Information Reference Signal
CSI-SINR	Channel State Information-Signal to Interference plus Noise Ratio
EMF	Electro-magnetic field
ES	Edge server
FSPL	Free space path loss
GSP	Graph signal processing
ICO	Intelligent cell optimization
IF	intermediate frequency
IIoT	Industrial Internet of Things
IMTC	Intelligent Machinery Technology Center
LOS	Line-of-sight
MCS	Modulation scheme and Coding Scheme
MEC	Mobile edge computing
MIMO	Multiple Input Multiple Output
MSE	Mean square error
NLOS	Non-line-of-sight
OLSM	Open-Loop Spatial Multiplexing
PDP	power delay profile
PLE	Path loss exponent
QAM	Quadrature Amplitude Modulation
RAN	Radio access network
REM	Radio environment map
RF	Radio Frequency
SINR	Signal-to-Interference-plus-Noise Ratio
SS-RSRP	synchronization signal reference signal received power
SSS	Secondary Synchronization Signal
TSP	Topological Signal Processing
UE	User equipment
VNF	Virtual network function
VUCA	Virtual uniform circular array antenna

Table of Contents

1 Introduction

The goal of this deliverable is to report the activities conducted within Tasks T3.1 and T3.2 of WP3. The main goal in T3.1 was to develop a realistic propagation model in an industrial environment, supported by an intensive measurement campaign. An effective channel sounder has been developed and illustrated in Section 2. In particular, a novel variant of the virtual uniform circular array antenna (VUCA) for sub 6 GHz measurements has been used at the receiver side for the measurement taken at 3.7 GHz and 28 GHz. A specific feature of the adopted system is to measure not only delay parameters but also angular – i.e. spatial – information. The measurements are illustrated in Section 3, and include path loss and delay spread models in both LOS and NLOS conditions.

Besides channel modelling, a further goal of T3.1 was also to develop algorithms to estimate a connectivity map, starting from sparse measurements. An algorithm has been developed based on a novel approach, denominated Topological Signal Processing (TSP), which makes use of higher order graphs (more precisely, simplicial complexes). The algorithm has been tested on simulated data obtained using a ray-tracing software. A description of the proposed algorithm is reported in Section 4, together with some preliminary results. The goal, in the near future is to expand these preliminary analysis and run the algorithms on real measurements taken at Taiwanese industrial sites, to test the capabilities of the algorithms.

In parallel, the objective of task T3.2 is to set-up an application-centric design able to allocate resources in order to enable the production process to proceed smoothly. This requires remote control of the whole process, including the RAN, MEC and core network. An optimal procedure for allocating resources in the edge cloud, including communication, computation and caching resources has been proposed and developed. The results are reported in Section 5. Capacity dimensioning and optimal placement of radio access points in an industrial environment, with specific reference to the Taiwanese site, have been analyzed and reported in Section 6. Finally, Section 7 reports some preliminary considerations about the network monitoring, including RAN, edge cloud and core networks.

1.1 Risk assessment and impact of COVID-19 crisis

While some of the activities within Work Package 3 only require theoretical efforts and algorithm development, other activities like the channel measurements at BOSCH facilities were heavily impacted by the COVID-19 crisis. The measurements were initially planned for the second half of 2020, but access to the factories was limited to essential workers and it was therefore impossible to conduct the measurements as planned. Despite having to delay the measurements, the channel sounder setup was fully developed, and the measurement scenarios and procedures were planned in time. 5G CONNI partners BOSCH and HHI actively monitored the pandemic situation, and the measurements were conducted in March 2021, as soon as access to the facilities was granted. Besides the measurements initially planned at 3.7 and 28 GHz, the consortium was able to conduct additional measurements at 300 GHz. While the data gathered during the campaign is enough to fulfill the project goals, discussions about an additional measurement in a factory in Taiwan are ongoing.

Due to the delayed measurement, the data evaluation and parameter estimation was also delayed. Large-scale parameters at 3.7 and 28 GHz were already estimated for all scenarios. Evaluation of the measurement results at 300 GHz and estimation of angle-of-incidence information is ongoing and will be finished in Q3 of 2021.

2 Channel sounding systems

A major item within task T3.1 is the investigation of the radio propagation conditions in the industrial environments, which are targeted by the project. Although the 3GPP TR 38.901 channel model has recently been extended with an Indoor Factory scenario, both the vast variety of different industrial environments and their distinctions from those environments for which the standard channel models have been developed mandate further research. In order to gain deeper insights into the radio propagation conditions in industrial deployments, a thorough channel measurement campaign was conducted at a BOSCH manufacturing facility using a channel sounder setup developed by HHI.

2.1 State of the art

2.1.1 Instrument-based time-domain channel sounder

The channel sounder setup is based on advanced test and measurement equipment and specific components developed by Fraunhofer HHI and uses the principle of time domain channel sounding. By using distributed, untethered reference clocks at the transmitter and receiver, the setup allows to conduct measurements in a highly flexible manner, without the need for a wired connection between transmitter and receiver. At the receiver, a virtual uniform circular array antenna (VUCA) is used that enables the estimation of angle-of-incidence information by applying the CLEAN technique with real-valued beamspace MUSIC as a DoA estimator. Over the last years, this setup has been used in a number of measurement campaigns with great success, mainly at 28 and 67 GHz. For the 5G CONNI project, a novel variant of the VUCA for sub 6 GHz measurements, specifically at 3.7 GHz, was developed. Figure 1 shows a block diagram of the channel sounder setup.

The transmitter comprises of at least a vector signal generator, a reference clock, a power amplifier and a transmit antenna, typically an omni-directional antenna like a bi-cone. Using a Rohde & Schwarz SMW200A, the sounding signal with a bandwidth of up to 2 GHz can be generated directly at RF frequencies up to 43 GHz. By using external up-converters, the frequency can be extended, currently up to 320 GHz.

A complex periodic Frank-Zadoff-Chu sequence is chosen as sounding signal for its optimal correlation properties. By an iterative optimization procedure, the crest factor could be reduced from 2.6 dB to an extremely low value of 0.3 dB. This allows for a low power back-off and highest transmit power. Depending on the frequency band and used power amplifier, the total transmit powers are between 27 and 34 dBm.

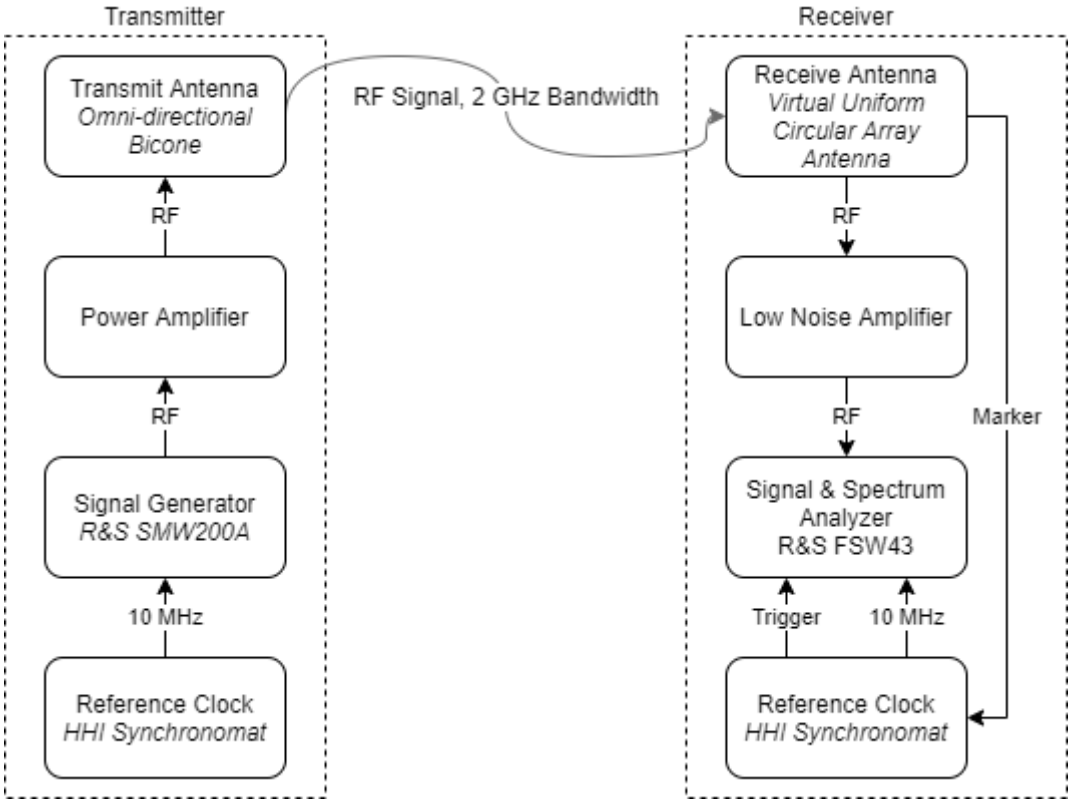

Figure 1: Block diagram of the channel sounder setup

On the receiver side, the setup comprises of at least a receive antenna, usually a *Virtual Uniform Circular Array Antenna*, a signal & spectrum analyzer, and a reference clock. In most cases, a low noise amplifier is also included. Similar to the transmitter, the signal & spectrum analyzer used in this setup (Rohde & Schwarz FSW43) allows the direct sampling of up to 2 GHz wide signals at frequencies up to 43 GHz, extendable by external down-converters. The reference clock now only provides a 10 MHz reference signal to the spectrum analyzer, but also triggers the receiver coherently to the rotation of the VUCA.

The setup is proven to provide excellent performance in terms of dynamic range, maximum measurable path loss and flexibility in several measurement campaigns in different scenarios. This is achieved by leveraging high-performance laboratory equipment and by exploiting the correlation and averaging gain of the chosen sounding signal. By comparing model simulations and verification measurements at 25 GHz, this digital correlative time domain channel sounder was demonstrated to achieve a close-to-optimum path loss dynamic range of 83.2 dB in a typical parametrization of the setup with a maximum measurable path loss of 143.2 dB.

2.2 Setup used for the measurements

The setup that was used for the measurements in the 5G CONNI project was similar to the setup described previously. At 3.7 and 28 GHz, the channel sounding sequence was generated directly at the RF frequencies with a bandwidth of up to 2 GHz. It was amplified to a total transmit power of 29 dBm at 3.7 GHz and to 30 dBm at 28 GHz and transmitted using a vertically polarized omni-directional bicone antenna. In addition to 3.7 and 28 GHz, at several locations, measurements were also conducted at 300 GHz. Here, the sounding signal was generated at an intermediate frequency (IF) of 12 GHz and fed to an external upconverter, where it was mixed with a 288 GHz carrier to produce the RF signal at 300 GHz. This signal was then transmitted using an open waveguide antenna. The frequency extension is described in

greater detail in subsection 2.2.1.1. A distributed reference clock (*Synchronomat* by Fraunhofer HHI)

At the receiver side, the signal was captured using a virtual circular array antenna (VUCA) with a vertically polarized omni-directional bicone antenna element at 3.7 and 28 GHz, and using a sectoral horn antenna (E-plane horn) at 300 GHz. A signal & spectrum analyzer was used to capture the signal directly at 3.7 and 28 GHz. At 300 GHz, the received signal was first fed through a frequency extender, where it was down-converted to an IF of 6.6 GHz. Baseband samples with a resolution of 16 bit were streamed to a connected PC and stored there. Also included in the receiver setup is another reference clock that enables coherent triggering of the signal analyzer. By continuously sampling the channel over a full rotation of the VUCA and averaging the CIR snapshots, the effects of small scale fading can be mitigated. This type of antenna also allows the estimation of spatial information by applying the CLEAN technique with the real-valued beamspace MUSIC (RB-MUSIC) algorithm as direction of arrival (DoA) estimator, which is explained in subsection 2.2.1.1.

Angle-resolved measurements in azimuth direction at 300 GHz were enabled by mounting the receiver on a precision rotation stage (Physik Instrumente M-061.DG) and rotating it in steps of 15 ° from -180 ° to +180 ° resulting in a total number of 25 angles measured.

Prior to the measurements, the reference clocks at Tx and Rx are synchronized. After a back-to-back calibration using a 60 dB attenuator, all cabled connections between Tx and Rx are removed, allowing completely untethered measurements. The receiver is also equipped with an uninterruptible power supply (UPS), that allows it to run for about three hours without being connected to an external power source.

A complex, periodic Frank-Zadoff-Chu (FZC) sequence was chosen as sounding signal for its optimal correlation characteristics. For the measurements in the first scenario, the VUCA was not rotating and therefore acting as a simple omni-directional antenna. Here, the sounding bandwidth was 2 GHz at both 3.7 and 28 GHz with a sequence duration of 50 µs. In the second and third scenario with the rotating VCA, the sounding bandwidth at 3.7 GHz was 400 MHz with a sequence duration of 250 µs and 2 GHz with a sequence duration of 50 µs at 28 GHz. This is to accommodate the slower rotational speed of 120 rotations per minute (RPM) at 3.7 GHz versus 1200 RPM at 28 GHz. Using these parameters, a total number of 2000 virtual array elements at 3.7 GHz and 1000 elements at 28 GHz was realized with a total acquisition time of 500 ms at 3.7 GHz and 50 ms at 28 GHz. The sounding sequence for 300 GHz channel measurements had a length of 100 µs and a bandwidth of 2 GHz. A set containing of 250 sequence periods is sampled for each measurement which leads to a total acquisition time of 25 ms.

2.2.1 Virtual Uniform Circular Array Antenna

In order to not only obtain delay parameters of the investigated radio propagation channels but also angular – i.e. spatial – information, spatial sampling must by applied at either the transmitter side or the receiver side of the channel sounder, or both. Many different approaches to this task have been reported in literature, including mechanically scanned directional antennas, different switched or phased array topologies as well as synthetic aperture techniques. Each of these techniques has its specific advantages and limitations that indicate applicability in a specific environment or measurement setup. For example, mechanically scanned antennas are easy to implement and entail no additional requirements in the receivers that are used, shifting most of the complexity to post processing of the acquired measurement data. However, their generally slow measurement speed makes them suitable mostly for static environments. On the other hand, phased or switched arrays in which spatial sampling is performed by a

large number of antenna elements allow for much shorter measurement durations but are associated with a much higher hardware and calibration effort and generally higher costs. Synthetic aperture or virtual array approaches constitute a compromise between these two extremes by sequentially sampling an aperture as would have been created by a full discrete array by mechanical translation of a single antenna element instead. Depending on the configuration of the considered aperture, this spatial sampling process may be implemented quite efficiently.

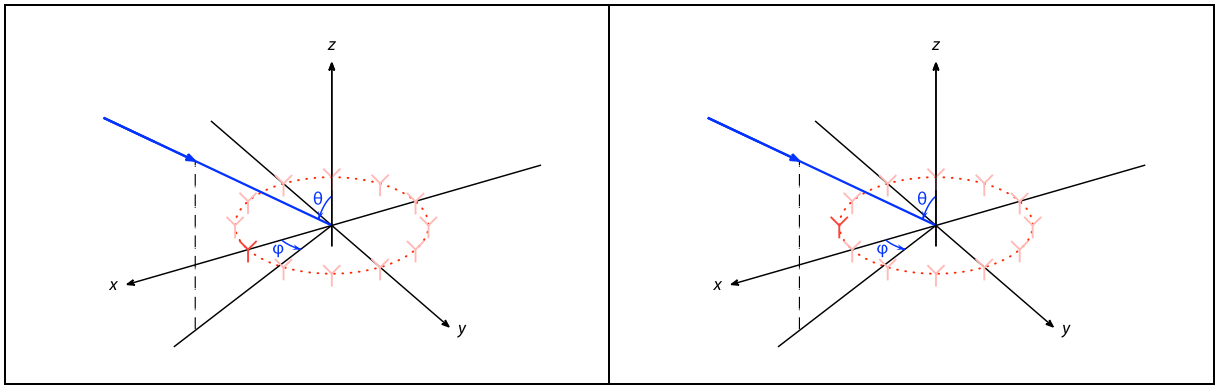

Figure 2: Virtual Array

In this channel sounder setup, the Virtual Uniform Circular Array approach reported in [NGU16] and illustrated in Figure 2 is used at the receiver side for the measurement taken at 3.7 GHz and 28 GHz. It is based on an omnidirectional receive antenna element mounted on a rotating fixture with defined displacement from the rotational center, thus enabling it to move along a circular trajectory. By synchronizing rotation speed to the sounder's stimulus signal period, a predetermined number of periods of the signal may be captured continuously during one revolution of the receive antenna rotator with well-known rotation angles for each of the signal periods. Each signal period and the instantaneous channel impulse response estimated from it corresponds to one virtual antenna element on the sampled circular aperture. The data obtained in this fashion may then be further processed by conventional array signal processing.

The VUCA approach offers several advantages: Firstly, by employing a single omnidirectional antenna, the measurement system's RF characteristics (antenna pattern, phase, attenuation, etc.) do not vary significantly over antenna position, considering that the errors introduced by mechanical RF rotary joints are bounded and the system may be designed rotationally invariant otherwise. Usage of an omnidirectional antenna element also allows for immediate extraction of delay-domain and overall channel characteristics without the need for deconvolution of the antenna's spatial response. Secondly, even short measurement durations result in significant oversampling of the spatial aperture benefitting the multipath-component estimation algorithms applied to the captured channel responses. As described above, a typical parametrization at 28 GHz results in 1000 virtual antenna elements with 50 ms of measurement duration.

It should be noted, however, that due to the two-dimensional configuration of the VUCA, it incurs aliasing either of the half-space above or below the aperture plane, i.e. unresolvable ambiguities in elevation angle.

2.2.1.1 Angle-of-Incidence estimation using RB-MUSIC

Estimation of discrete multipath components is based on the P-component discrete impulse response signal model

$$h(\tau,\phi,\theta) = \sum_{i=1}^{P} \boldsymbol{\alpha}_i \delta(\tau-\tau_i)\delta(\phi-\phi_i)\delta(\theta-\theta_i),$$

where $\boldsymbol{\alpha}$ denotes complex path attenuation, τ the path delay and ϕ, θ azimuth and elevation of arrival, respectively.

Suppose a VUCA captures M periods of the sounder's stimulus signal from which M complex-valued, instantaneous delay-domain channel impulse responses $\hat{h}_i(\tau)$ are estimated. Under a narrowband assumption the array manifold phase weight of the i-th element of the radius r VUCA is given by

$$a_i(\phi,\theta) = e^{jk_0 r \sin(\theta)\cos(\phi-\frac{2\pi}{M}i)},$$

with k_0 being the free-space wave number at the impinging signal's center frequency. Thus, the estimated channel impulse responses are considered the result of the convolution

$$h_i(\tau) = a_i(\phi,\theta) * h(\tau,\phi,\theta).$$

By analyzing the averaged power delay profile

$$APDP(\tau) = \frac{1}{M}\sum_{i=0}^{M-1} |h_i(\tau)|^2 \ ,$$

for example by local maximum search, one may identify the delay taps τ_i. Then, for each delay tap, the complex array response

$$\hat{\boldsymbol{r}}(\tau_i) = [\hat{h}_0(\tau_i), \dots, \hat{h}_{M-1}(\tau_i)]$$

may be extracted for further processing.

Estimation of one or more angular components contained within a delay tap can be performed with the well-known MUSIC algorithm. However, since the number of virtual antenna elements is large, this algorithm is computationally expensive. Hence, the real valued beamspace MUSIC variant of [MAT94] is used. It reduces complexity by exploiting the specific properties of circular array geometries. Firstly, it uses a much more compact beamspace representation of the data which is, secondly, transformed to be purely real-valued.

2.2.2 Frequency extension up to 300 GHz

The frequency extensions are based on both commercial off-the-shelf and specific components developed by Fraunhofer HHI and Fraunhofer IAF. For the 300 GHz extension, in order to achieve single sideband up-conversion, a 3 dB quadrature hybrid (Marki Microwave QH-0R714) is used to generate 0° and 90° phase shifted variants of the IF signal, which is then up-converted within the THz IQ transceiver module (M238RTRH by Fraunhofer IAF). The final RF frequency can be between 270 and 320 GHz, depending on the LO frequency. With the current setup, a lower sideband suppression of 15 dB can be achieved and it can probably be further increased by calibration of the IQ mismatch. A power amplifier developed by Fraunhofer IAF is used to amplify the RF signal to a total power of 3 dBm.

A functional block diagram of the THz IQ transceiver module is shown in Figure 3. The module supports an external local oscillator reference signal between 7.5 and 8.9 GHz. The signal is split after the frequency multiplier MMIC (X12) by a 3-dB waveguide coupler. The two synchronous signals are input to the Tx respectively Rx MMIC, which multiply them to a local oscillator frequency in the band from 270 to 320 GHz. The fundamental broadband mixer uses a direct conversion architecture. The in-phase (I) and quadrature (Q) baseband signals can have a

bandwidth of more than 20 GHz. The Tx MMIC integrates a broadband medium power amplifier and the Rx MMIC integrates a high gain low noise amplifier. The employed MMICs were implemented using a 35 nm metamorphic HEMT technology with an $In_{0.52}Al_{0.48}As/In_{0.80}Ga_{0.20}As$ channel grown on 4" GaAs wafers.

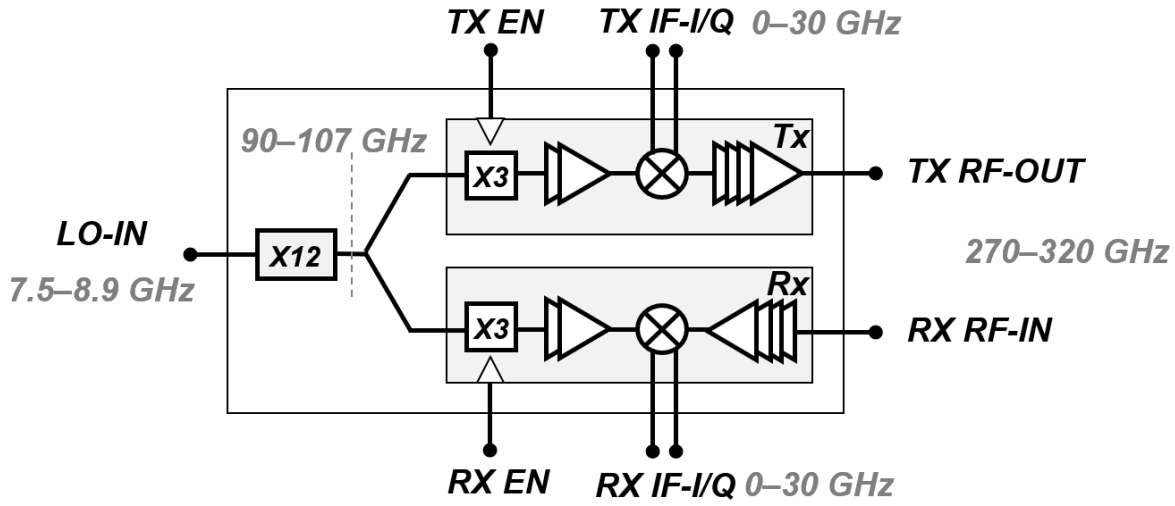

Figure 3: Functional block diagram of the 300 GHz transceiver waveguide module. Grey components are realized as individual MMICs.

At the receiver side, a similar heterodyne principle as at the transmitter is used, but in a double sideband configuration. Single sideband down-conversion using a quadrature hybrid is possible, but no gain in precision and accuracy is expected. In this case, the LO is generated at a frequency of 8.15 GHz and multiplied by 36 to 293.4 GHz, resulting in an IF of 6.6 GHz for the upper sideband signal which is sampled by a signal and spectrum analyzer.

The LO and IF frequencies at transmitter and receiver are chosen in a way that no unwanted images or LO signals generated by the transmitter side appear into the upper sideband of the receiver. In general, the IF at the transmitter side should be chosen quite high, to separate LO feedthrough and lower sideband image from the signal well, whereas at the receiver side the IF frequency should be as low as possible, to ensure the best sensitivity of the 300 GHz IQ mixers. Since the THz transceiver supports an IQ bandwidth of more than 20 GHz, extremely wide-band channel sounding would be possible. Theoretically, a direct IQ modulation and demodulation should also be possible with the setup, which was not investigated so far.

Similar frequency extensions were also developed for 140-220 GHz.

3 Measurements and evaluation of measurement data

Using the channel sounder setup described in the previous section, an extensive measurement campaign at a BOSCH manufacturing facility was conducted by HHI. The data from these measurements will be used as input to the algorithms developed by 5G CONNI partner SAP, and to contribute to the further standardization of industrial channel models. A novel aspect of the investigations is the inclusion of spatial resolution in the low-frequency measurements at 3.7 GHz, providing for example angle-of-incidence information, and the measurements at 300 GHz.

3.1 Measurement Scenarios and Procedure

The measurements were conducted inside of an industrial production hall with an outer dimension of approximately 100 by 50 meters and a ceiling height of about 5 meters. Over the whole production hall, the ceiling is packed with metallic cable and air ducts, limiting the usable height to about 3.5 meters. The hall is enclosed by a mixture of metallic and concrete walls to east and west, and by dry walls to adjacent conference rooms to north and south. Figure 4 shows a floor plan of the hall with the transmitter and receiver positions in the different scenarios.

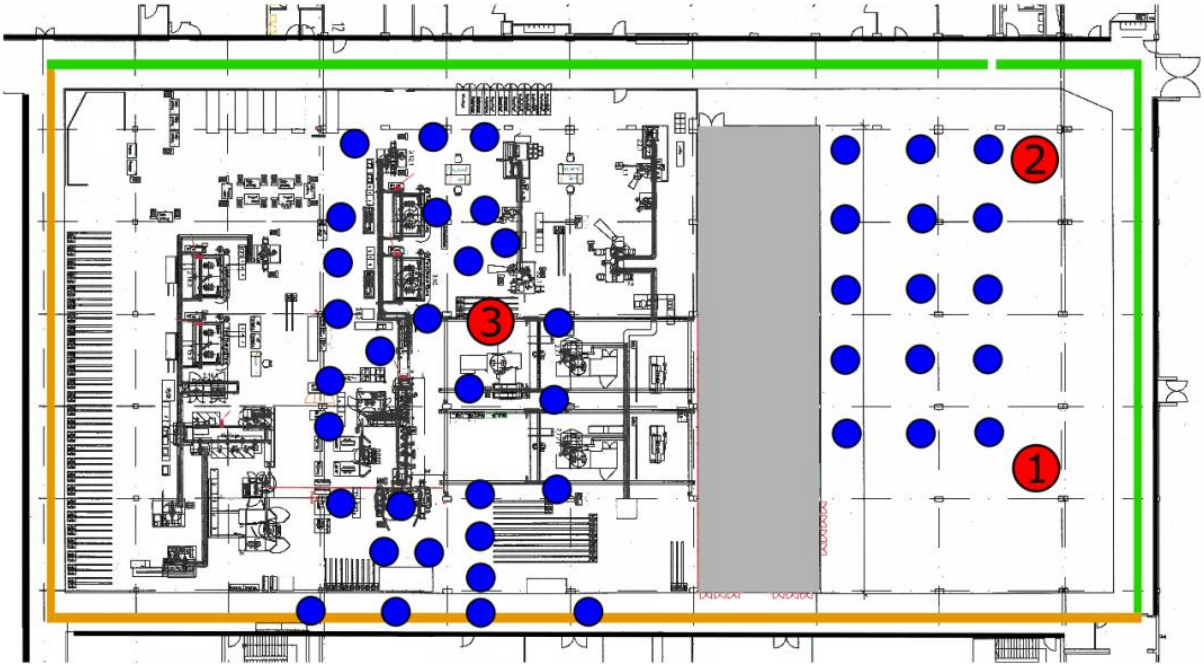

Figure 4: Floor plan with different measurement scenarios.

Three different scenarios were defined for the channel measurements. First, the mobile receiver was moved on a path along the perimeter of the hall that is used by automated guided vehicles (AGV) and pallet trucks to resupply the production machines and transport finished goods. For these measurements, the transmitter was set at position 2 in Figure 4 at a height of 2.7 meters above ground. The receiver was set up at a height of 2.2 meters above ground and was moved with a constant speed of 0.5 meters per second along the trajectory highlighted in green, yellow and orange in Figure 4. The trajectory spans 85 meters from east to west and 45 meters from north to south. A channel impulse response (CIR) snapshot was recorded every 15 cm. Approximately half of the measurement positions were line of sight while the other half was non-line of sight. Figure 5 shows the perimeter along the south side of the hall. In the first scenario, measurements were conducted only at 3.7 and 28 GHz.

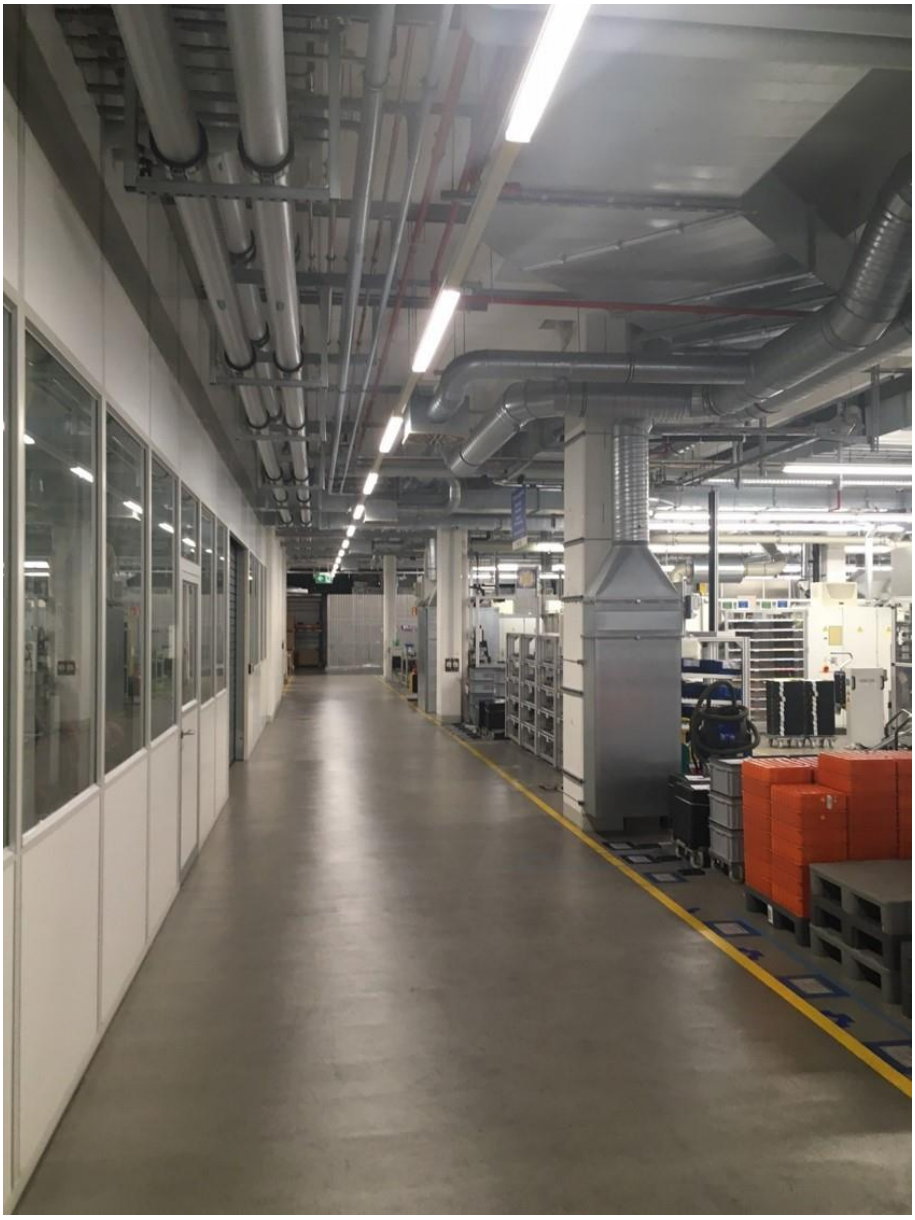

Figure 5: Perimeter scenario

The measurements in the second scenario were conducted in a storage and prototyping area in the east of the hall. This area is sparsely packed with robots, stored machines and work spaces. Concrete pillars are placed approximately 7.5 meters apart. The transmitter was consecutively placed at two locations (positions 1 and 2 in Figure 4) at a height of 2.7 meters above ground. The stationary receiver was placed at 15 locations on a 3x5 grid in an area of 10 by 20 meters at a height of 2.2 meters above ground. Of the 15 measurement points, 13 were line of sight and two were non-line of sight at Tx position 1, and 7 were line of sight and 8 were non-line of sight at Tx position 2. At every measurement point, 1000 CIR snapshots at 28 GHz and 2000 CIR snapshots at 3.7 GHz were captured. The minimal 3D distance between transmitter and receiver was 1.91 meters, the maximum 3D distance was 23.8 meters. Figure 6 shows transmitter and receiver in the storage area. In this scenario, measurements were conducted at 3.7, 28 and 300 GHz.

Figure 6: Storage and prototyping area.

For the third scenario, the measurements were conducted on the shop floor of the production hall. Here, the area is densely packed with machinery and robots, largely consisting of metal or with metallic surfaces. Enclosing the shop floor are partially windowed dry walls up to a height of approximately 2.5 meters. The transmitter was placed in the middle of the shop floor (position 3 in Figure 4) at a height of 2.7 meters above ground. The stationary receiver was placed at 30 positions throughout the shop floor at a height of 2.2 meters above ground. Of the 30 measurement points, 7 were line of sight and 23 were non-line of sight. As with the measurements in the second scenario, 1000 CIR snapshots at 28 GHz and 2000 CIR snapshots at 3.7 GHz were captured at every measurement point. The minimal 3D distance between transmitter and receiver was 3.1 meters, the maximum 3D distance was 26.9 meters. Figure 7 shows transmitter and receiver during calibration on the shop floor. In this scenario, 300 GHz measurements were conducted in addition to 3.7 and 28 GHz at five positions.

Figure 7: Shop floor scenario.

The three scenarios were chosen to represent typical use cases for wireless connectivity in an industrial environment: On the perimeter, AGVs need to be controlled and supervised and instructions can be provided to workers on pallet trucks. In both the prototyping and storage area and on the shop floor, a reliable wireless connection allows the flexible and rapid reconfiguration of machines and workplaces.

3.2 Measurement results and evaluation

In order to estimate the large-scale parameters, power delay profiles (PDPs) were derived from the CIRs captured by the channel sounder setup at 3.7 and 28 GHz. For the measurements conducted in the first scenario, instantaneous power delay profiles (IPDPs) were derived for every measurement point. To minimize the effects of small-scale fading, four consecutive IPDPs were averaged, corresponding to average power delay profiles (APDPs) for every 60 cm of the trajectory. Evaluation of the APDPs in scenario 1 showed that the dynamic range was only high enough to estimate large-scale parameters for the parts of the trajectory highlighted in green in Figure 4. This resulted in a minimal 3D distance between Tx and Rx of 3.1 meters and a maximum 3D distance of 78.5 meters.

For scenarios 2 and 3, 2000 and 1000 CIR snapshots were captured, respectively, at 3.7 and 28 GHz at every measurement point. Based on these CIR snapshots, APDPs were derived.

Prior to the estimation of large scale parameters, an evaluation threshold of 30 dB relative to the strongest component of each APDP was applied. Local maxima in the APDPs were then identified and used to estimate path loss and delay spread for each scenario in LOS and NLOS condition separately. Furthermore, for the measurements in LOS, the ratio between the LOS component and all other specular components was evaluated by comparing the magnitude of the first identified component of the APDP to the sum of magnitudes of all other identified components. Figure 8 shows a sample APDP of a measurement conducted at 28 GHz in scenario 2. The line of sight component is received at a delay of 83.5 ns with a magnitude of -

89.56 dB and several multipath components are identified up to a delay of 302 ns. The noise floor, or median of the APDP, has a magnitude of -127.3 dB and all multipath components with a magnitude of less than 10 dB above the noise floor (absolute threshold) are discarded. Furthermore, the relative evaluation threshold is also displayed in Figure 8.

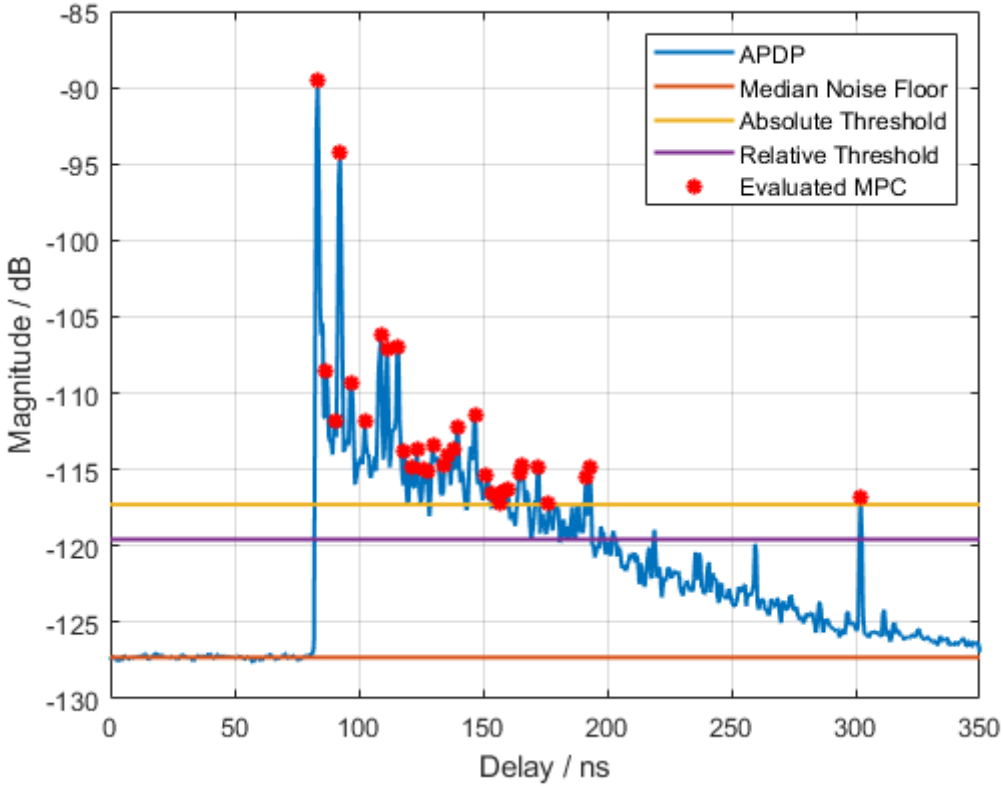

Figure 8: Sample APDP at 28 GHz in scenario 2 in LOS condition

By comparing the APDPs of back-to-back measurements before and after each scenario, the drift of the distributed reference oscillator could be evaluated. The results show that the reference clock drifted less than 10 ns over the measurement period of 60 to 90 minutes per scenario with a single outlier where the overall drift was 22 ns.

3.2.1 Path Loss

The path loss was evaluated based on the accumulated powers of the identified local maxima in the APDPs separately for LOS and NLOS. Figure 9 shows the results of the evaluation in LOS condition at 3.7 and 28 GHz. The measurement points at 3.7 GHz are denoted by circles, those at 28 GHz by triangles. Results for scenario 1 are colored blue, red for scenario 2 and yellow for scenario 3. Additionally, the free space path loss (FSPL) is displayed as a dashed black line. The path losses for both frequencies in all scenarios are about 3 dB lower than FSPL with a couple of outliers at 3.7 GHz in the highly dense scenario 3. Here, the difference to FSPL is more than 8 dB.

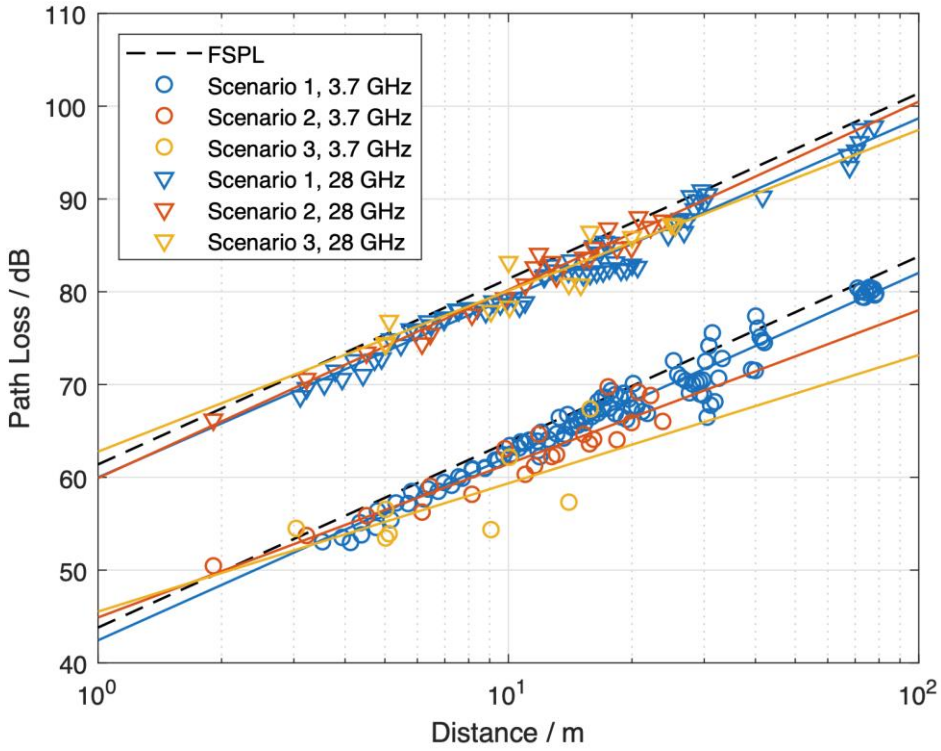

Figure 9: Path loss in LOS condition.

The results of the evaluation in NLOS are shown in Figure 10 with the same symbols and colors as in LOS. Here, it can be seen that the path losses in scenario 1 are very close to FSPL, both at 3.7 and 28 GHz. This can be explained by the fact that, while the direct LOS path was blocked, the area between Tx and Rx was much less cluttered than in scenarios 2 and 3, where the path loss is considerably higher than FSPL.

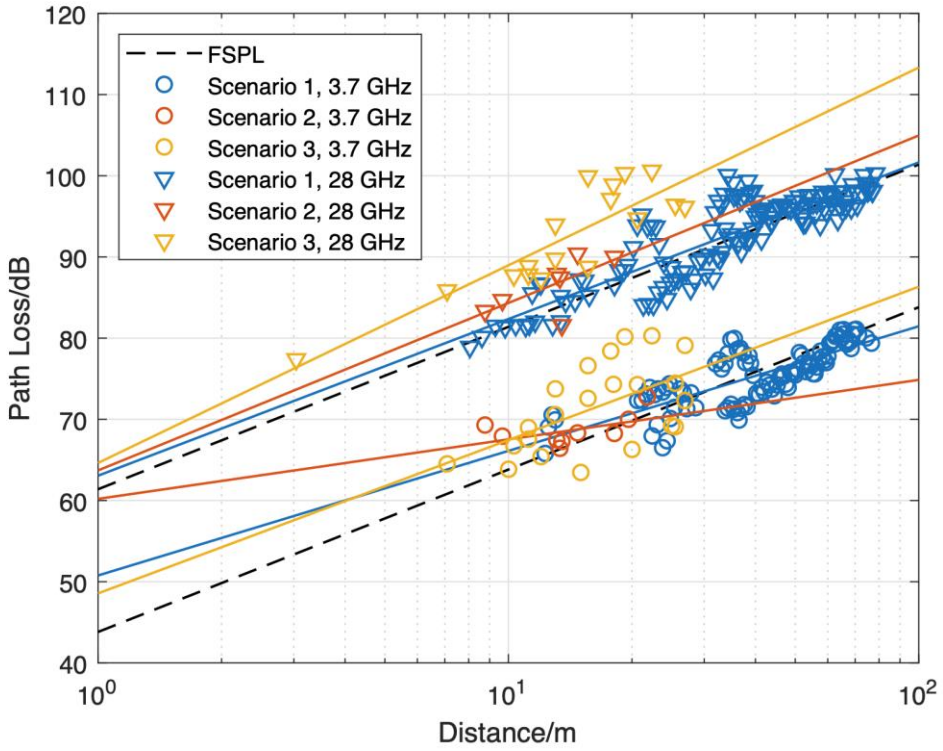

Figure 10: Path loss in NLOS condition.

For both LOS and NLOS, floating intercept (FI) and fixed reference (FR) path loss model parameters according to

$$PL(d) = PL_0(d_0) + 10n\log_{10}\left(\frac{d}{d_0}\right) + \mathrm{X}_\sigma$$

were derived using least squares fitting. d_0 is the reference distance of 1 m, d is the Tx-Rx 3D distance, n is the path loss exponent (PLE) and X_σ is the lognormal random shadowing variable with 0 dB mean and standard deviation σ. $PL_0(d_0)$ is the modelled FI path loss at reference distance d_0 for the FI model and fixed to FSPL at d_0 for the FR model. The results of the least squares fitting are shown in and the FI models are also visualized in Figure 9 and Figure 10. In scenario 2 at 3.7 GHz, the FI model shows a high path loss at reference distance with a shallow exponent, resulting in unrealistic path losses for distances outside of the underlying measurement results. This can be explained by the low number of NLOS positions in the second scenario, which all showed similar path losses at 3.7 GHz, regardless of their distance.

3.2.2 K-factor

Besides path loss, the K-factor, or ratio between the LOS component and all other specular components, according to

$$K = P^{LOS} - 10\log_{10}\left(\sum_{n=1}^{N} 10^{\frac{P_n}{10}}\right)$$

was evaluated. P^{LOS} is the power of the LOS component, N is the number of specular components with a power of P_n. The 3GPP TR 38.901 channel model lists values between 7 and 9 dB, depending on the scenario. In Table 1, the mean values and standard deviations are shown. Additionally, Figure 11 displays the cumulative distribution function (CDF) of the K-factor in the different scenarios.

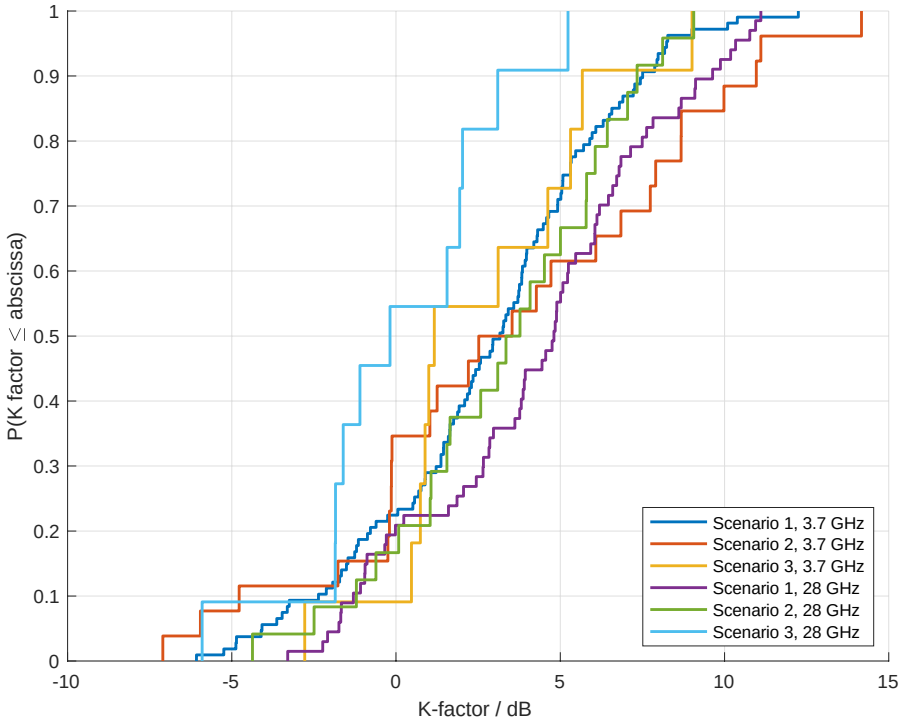

Figure 11: CDF of K-factor in LOS condition.

The mean K-factor is decreasing from 4.28 dB at 3.7 GHz and 6.22 dB at 28 GHz in scenario 1 to 2.65 dB at 3.7 and 0.12 dB at 28 GHz in scenario 3. This can be explained by the increasing density of reflective clutter in the scenario and highlights the unique nature of industrial environments where in some instances, the combined power of all non-line of sight multi-path components can be greater than the line of sight power.

3.2.3 RMS Delay Spread

The root mean square (RMS) delay spread was calculated based on the identified local maxima in the APDPs after an evaluation threshold of 30 dB relative to the strongest MPC was applied. In Table 1, the statistical parameters mean, median, standard deviation σ and 95%-quantile are shown. In Figure 12 and Figure 13, the CDFs of the delay spread are shown in LOS and NLOS condition, respectively.

At 28 GHz, the mean RMS delay spread in LOS condition is 5 to 10 ns lower than in NLOS condition with relatively constant values across all three scenarios. However, at 3.7 GHz, the mean RMS delay spread in scenarios 1 and 3 is almost twice as large in NLOS as in LOS, which can be explained by the large number of multi-path components in this highly reflective environment. Generally, it can be seen in the CDFs that higher delay spreads occur in the first scenario due to the higher distances between transmitter and receiver.

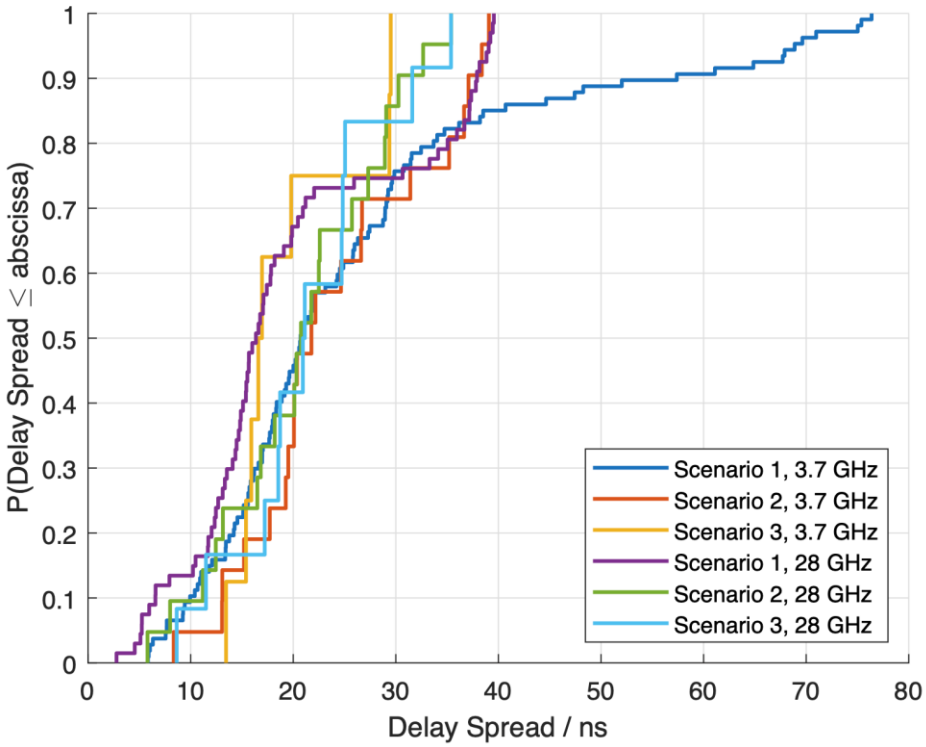

Figure 12: CDF of RMS delay spread in LOS condition.

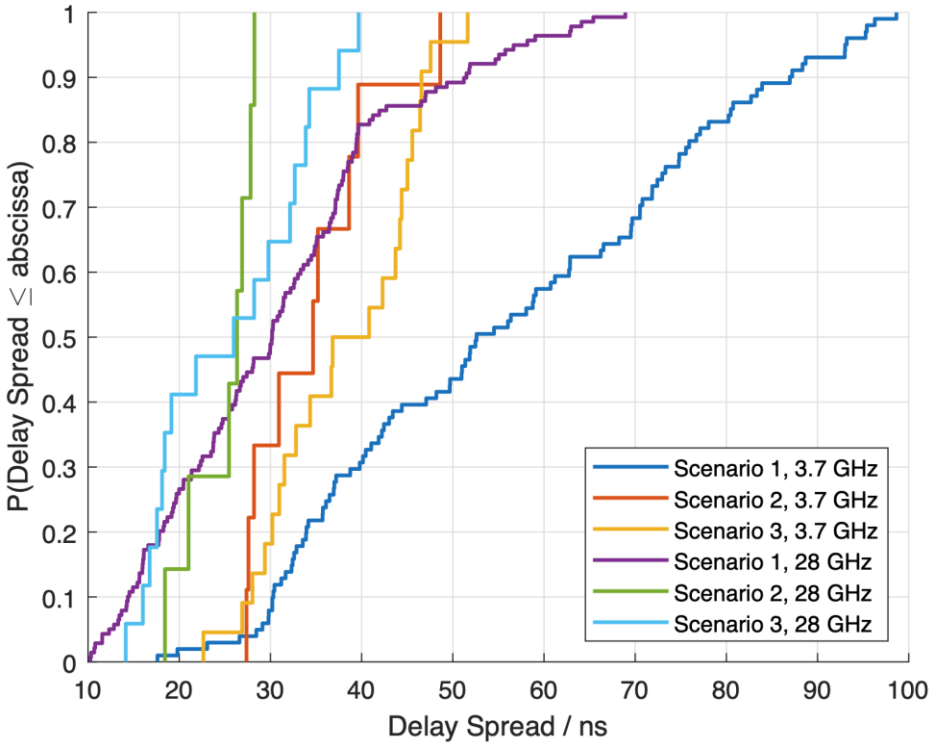

Figure 13: CDF of RMS delay spread in NLOS condition.

3.2.4 Estimated Large Scale Parameters

The estimated large scale parameters (Path Loss, K-factor and RMS Delay Spread) in all three scenarios are summarized in the following table.

Table 1: Estimated Large Scale Parameters

Scenario	**Perimeter (Scenario 1)**				**Storage Area (Scenario 2)**				**Shop Floor (Scenario 3)**			
Frequency	**3.7 GHz**		**28 GHz**		**3.7 GHz**		**28 GHz**		**3.7 GHz**		**28 GHz**	
LOS/NLOS	**LOS**	**NLOS**	**LOS**	**NLOS**	**LOS**	**NLOS**	**LOS**	**NLOS**	**LOS**	**NLOS**	**LOS**	**NLOS**
Path Loss (FI)												
$PL_0(d_0)$ (dB)	42.44	50.77	59.99	63.06	44.90	60.21	59.92	63.71	45.53	48.56	62.77	64.63
n	1.98	1.53	1.94	1.93	1.66	0.73	2.03	2.06	1.38	1.89	1.73	2.44
σ (dB)	1.39	2.27	1.21	2.60	1.69	1.61	1.04	2.53	3.45	4.41	1.82	3.20
Path Loss (FR)												
$PL_0(d_0)$ (dB)	43.81	43.81	61.38	61.38	43.81	43.81	61.38	61.38	43.81	43.81	61.38	61.38
n	1.88	1.96	1.82	2.04	1.75	2.14	1.90	2.27	1.57	2.27	1.86	2.71
σ (dB)	1.43	2.41	1.28	2.62	1.70	2.46	1.10	2.54	3.49	4.46	1.85	3.26
K-factor												
Mean (dB)	4.28	-	7.22	-	3.51	-	3.28	-	2.65	-	0.12	-
σ (dB)	3.92	-	7.68	-	5.51	-	3.47	-	3.27	-	3.04	-
Delay Spread												
Mean (ns)	26.27	56.04	19.88	30.82	24.12	34.54	20.93	24.89	19.62	38.11	21.53	25.65
Median (ns)	20.71	52.61	16.37	30.19	21.77	34.68	20.75	26.34	16.78	38.82	21.03	25.97
σ (ns)	17.28	21.37	10.99	13.47	9.09	7.02	8.07	3.72	6.31	8.15	7.57	8.41
95% Conf. (ns)	68.99	93.10	39.08	57.49	38.69	48.63	33.89	28.24	29.51	49.19	35.00	38.92

3.3 Outlook on further evaluation

While the large scale parameters at 3.7 and 28 GHz are already extracted for all scenarios, the data gathered during the measurement campaign allows further evaluation of the propagation characteristics of the industrial environment. The next step will be to incorporate angle of incidence information by calculating angular power profiles based on the channel impulse responses gathered at 3.7 and 28 GHz in scenarios 2 and 3. These power profiles will then be used to estimate the angular spread of arrival.

Additionally, the measurements at 300 GHz in scenarios 2 and 3 will be thoroughly evaluated. Both large scale parameters and angle of incidence information can be extracted and later compared to the results at 3.7 and 28 GHz.

3.4 Comparison between simulation and model results

In order to draw a comparison between the simulation results generated using Ranplan software tool running on the 3D model of IMTC premises and the HHI model built from the measurements conducted at the Bosch factory using HHI channel sounder, a simulation was set up to check whether the two sets of data could match. One gNodeB with a single, omni-directional antenna was placed and used to predict the SS-RSRP (Synchronization Signal Reference Signal Received Power) at 3.7 GHz with a bandwidth of 100 MHz. As it is not possible to extract

channel impulse responses, power delay profiles or any type of statistical channel parameters from Ranplan, the SS-RSRP was the only viable parameter to evaluate the received signal strength and through that the path loss. Other large-scale parameters, like delay spread or K-factor, could not be compared.

Figure 14: Floor plan of the IMTC simulation setup in Ranplan

Figure 14 shows the floor plan of the IMTC simulation setup in Ranplan with a gNB at (x,y) = (-23,-8). As it was neither possible to extract the line of sight condition of measurement points nor the 3D model of the simulation, just the non-line of sight conditioned points along a line at y=-8 were used as NLOS data. Similarly, a gNB was set up at (x,y) = (-23,-1), and simulation points along a line at y=-1 were extracted as LOS data.

In Figure 15, the extracted SS-RSRP values are plotted over distances between 3 and 50m together with the HHI's model values based on the fixed reference path loss model in scenario 3 (Shop floor), and free-space path loss. As the simulated SS-RSRP values were converging to -67.76 dB at a distance between transmitter and receiver of 3m, this distance and RSRP value where chosen as reference. To represent free-space path loss, a model with an exponent of n=2 was selected, which is represented by the yellow line in Figure 15. By evaluating the measurements at the shop floor at 3.7 GHz, an exponent of n=1.57 in LOS and n=2.27 in NLOS condition was found. It has to be noted that the LOS model is only based on very few measurement points. By visually analyzing the LOS simulation results in Figure 15, it can be seen that the LOS model with n=1.57 is not a good fit. The simulation closely follows FSPL with a near constant offset of about 1 dB. Linear regression on the simulation results yields an exponent of n=1.91, which is much closer to the measurement-based model values of n=1.88 in scenario 1 and 1.75 in scenario 2, both of which are much less densely scattered with machinery as scenario 3. Generally speaking, it can be seen that both the simulation and measurement values yield higher received power and with lower path losses than that coming from a free-space path loss model. This can be explained by the highly reflective environment that can lead to constructive addition of signals at the receiver. Of course this statement has only limited validity, conditioned to the environments under analysis.

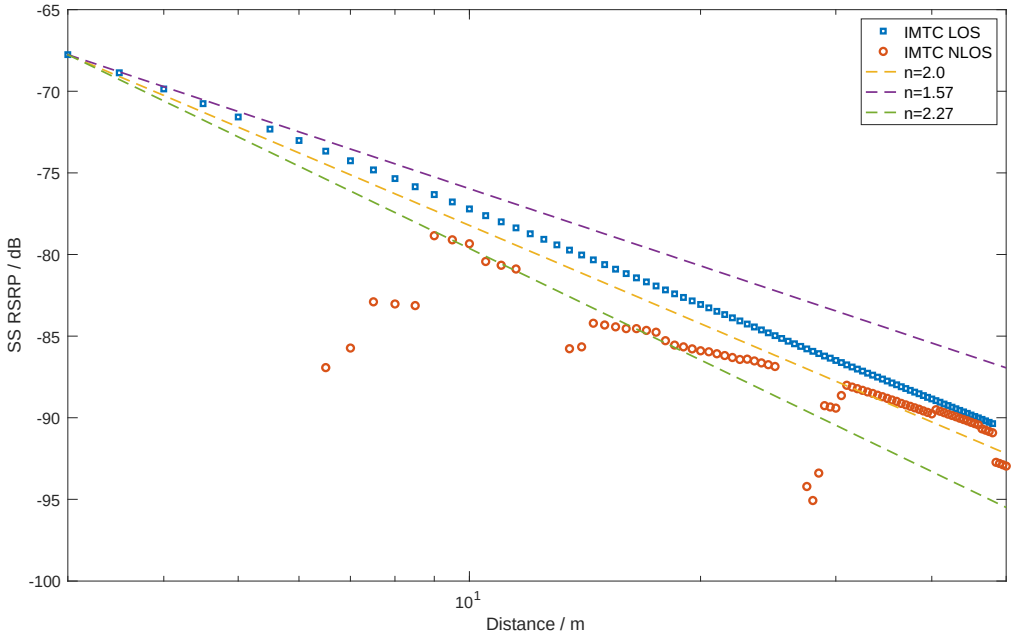

Figure 15: SS-RSRP values over distance with model parameters

Visually, the NLOS model with an exponent of n=2.27 based on the measurement data is a good fit for simulation results up to 25 meters except for a couple of outliers with a much higher path loss. Linear regression on the NLOS simulation results up to this distance show an exponent of n=2.21 that is very close to the NLOS model based on the measurement results. For higher distances, the NLOS simulation results draw near the LOS results. Linear regression over all NLOS simulation results give an exponent of n=2.07 that is very close to free-space path loss. From this comparison, we can state that a two-part model with a breaking point at a distance of about 25 meters would be a more suitable model.

In conclusion, due to the rather limited set of propagation properties that can be provided by Ranplan, a thorough comparison based on large-scale channel parameters between simulation and measurements is not possible. Comparison between measurement-based estimated path loss model exponents and simulated received signal strength reveal that, in LOS condition, Ranplan seems to more or less follow free-space path loss with just a few added multipath components. In NLOS condition, at least for distances up to 25m, the simulated received powers well match the model based on the measurements conducted in the highly dense shop floor scenario. For greater distances, the simulation results draw nearer to FSPL and to the LOS results. Generally speaking, using Ranplan, it would be desirable, if possible, to either set propagation parameters like path loss exponents, RMS delay spread, or K-factor, or to export the generated channels for external evaluation.

4 Connectivity map

One of the activities within T3.1 is devoted to build a connectivity map of performance parameters such as received signal strength (RSS), throughput, latency, etc. The goal is to reconstruct the values of such parameters from sparse measurements, over non-observed points in space and/or time. This reconstruction, or prediction, coupled with real measurements within the factory, could help private operators and/or factory owners, to dynamically adjust the network and prevent coverage holes, out-of-service events, high latency between two links, etc.

4.1 State of the art

4.1.1 Radio Environment Map

One of the topics most closely related to building a connectivity map is the concept of Radio Environment Map (REM) [PAR17].

[PAR17] O. Parzanchevski and R. Rosenthal, “Simplicial complexes: Spectrum, homology and random walks,” Random Struct. Algorithms, vol. 50, no. 2, pp. 225–261, 2017.

[PES14], [WEI13], [WEI13][WEI13][WEI13] i.e. the reconstruction of the EMF from measurements performed in a few locations in space [BAZ11], [WEI13], [YIL13] , [FAR16], [LI17], [ROM17], [HAN19]. The goal is to reconstruct, from sparse measurements, the field over the entire space of interest (e.g., the factory plant). This allows the operators to plan the installation of new Access Points (APs), whenever there are coverage issues, without the need to measure the EM over the entire space or, for instance, to enable a dynamic spectrum access and a cognitive usage of the radio resources [WEI13], [YIL13]. In [YIL13], different aspects of REM are presented, ranging from REM architecture to the actual methods. In addition, a comparison of different algorithms for REM reconstruction is presented. In [BAZ11], a sparsity-aware spline-based method is developed for spectrum cartography, with a distributed algorithm over a wireless sensor network. In [WEI13], the authors analyze the relationship between the REM accuracy and the number of samples used to reconstruct the REM. [FAR16] is the first work that analyzes the performance of a REM reconstruction method in presence of measurement errors. In [ROM17], a reconstruction algorithm is proposed, based on measurements taken by low-cost sensors, which introduce quantization distortion when transmitting the measurements to a fusion center. Finally, the authors of [HAN19] propose an interpolation algorithm based on the Kriging algorithm. One promising method, analyzed in [BAR18], hinges on Graph Signal Processing (GSP) to reconstruct the EMF from sparse measurements in an urban environment.

While all the above works are concerned with the estimation of a scalar field, such as for example the intensity of the e.m. field in every point in space, the goal of the activity carried out in T3.1 is to develop a technique to recover performance parameters associated to coupes of points, such as, for instance, the RSS at the receive side, as a function of the position of the transmitter, or the data rate between two points, etc. This task represents a challenging problem that goes beyond the capabilities of current methodologies. To tackle the problem, we resorted to the signal processing framework denominated Topological Signal Processing (TSP), developed by SAP, as a generalization of Graph Signal Processing (GSP). We now present the state of the art on GSP solutions for signal reconstruction based on sparse measurements, to finally present our extension based on TSP.

4.1.2 Recovery of flows data using Topological Signal Processing

The field of graph signal processing (GSP) has recently emerged as a powerful framework for the representation, processing and analysis of networks where signals are defined over the

vertices of a graph [SHU13], [ORT18]. A graph is represented by a set of nodes/vertices, connected through a set of edges/links. Two different vertices are connected through a link/edge, if a predefined relation exists between them, e.g. they are close to each other, under a given definition of distance. Note that, the metric used for the distance is not necessarily based on the Euclidean distance, but also on a measure of similarity/dissimilarity between the signals associated to the nodes of the graph [BAR18]. In particular, GSP deals with the problems of recovering the signals observed over all the nodes of the graph from sparse measurements. [DIL18] provides an overview of graph-based methods for sampling and recovery of graph signals. For example, the work in [CHE15] provides conditions that guarantee unique reconstruction of signals spanned over a subset of vectors composing the graph Fourier basis, proposing also a greedy method to select the sampling set in order to minimize the effect of sample noise in the worst-case. Reference [WAN15] exploited a smart partitioning of the graph in local sets and proposed iterative methods to reconstruct bandlimited graph signal from sampled data. The work in [TSI16] creates a conceptual link between uncertainty principle and sampling of graph signals, and proposes several optimality criteria (e.g., the mean-square error) to select the sampling set in the presence of noise. The work in [PUY16] provides an efficient design of sampling probability distribution over the nodes, deriving bounds on the reconstruction error in the presence of noise and/or approximatively bandlimited signals.

As already mentioned, a graph is built through the definition of a similarity measure to establish links between nodes. In [BAR18], a similarity measure based on EMF measurements is used to infer the topology of the graph, and REM reconstruction is performed through GSP tools. In this context, using graphs, one can measure the signal (e.g. EMF) over a subset of receiving nodes, generated by one or more base stations, and reconstruct the signal over the subset of unobserved nodes. Moreover, the measurements can be assumed to be corrupted by noise.

GSP tools are powerful, however, graph-based representations only encode pairwise relationship among data and are not always able to capture all the information present in interconnected systems that require a multiway (i.e., higher than pairwise) description, as suggested in [KLA09], [BEN18]. To overcome the limitations of graph-based representations, we can exploit tools from algebraic topology to handle multiway relations. Algebraic topology is a branch of mathematics that uses tools from abstract algebra to study a topological space, i.e. a set of points, along with a set of neighbourhoods. Topological Signal Processing (TSP) is a recently developed framework, which represents the general extension of GSP to the analysis of signals defined over higher-order structures, such as hypergraphs [ZHA20] or simplicial complexes [BAR20_2]. For example, while graphs are well appropriate to analyze signals defined over the nodes of a graph, when we deal with signals associated to the edges of a graph, as for example in the case of data flows, it is necessary to capture similarities between edge signals. As explained in [BAR20], to perform this operation properly it is necessary to simplicial complexes including triangles that encode three-way relations. More generally, the Topological Signal Processing framework can then be used to reconstruct (edge) signals defined over the links of a communication network, with typical examples including throughput and latency, all quantities that are associated to a pair of points, namely the transmit and receive sides. There are different works dealing with the analysis of edge signals, like [SCH18], [JIA19], [EVA09], [AHN10]. More specifically, in [SCH18] the authors introduced a class of filters to analyze edge signals based on the edge-Laplacian matrix [MES10]. A semi-supervised learning method for learning edge flows was also suggested in [JIA19], where the authors proposed filters highlighting both divergence-free and curl-free behaviors. Other works analyzed edge signals using a line-graph transformation [EVA09], [AHN10]. Random walks evolving over simplicial complexes have been analyzed in [MUK16], [PAR17], [SCH18_2]. In [MUK16], random walks and diffusion process over simplicial complexes are introduced, while in [SCH18_2] the authors focused on the study of diffusion processes on the edge-space by generalizing the well-known

relationship between the normalized graph Laplacian operator and random walks on graphs. In [BAR20_2], the authors developed a fundamental framework to analyze signal defined over simplicial complexes, a class of hypergraphs that is particularly appealing for its rich algebraic structure, showing how higher order structures, able to capture relationships among triplets of nodes, provide an advantage with respect to graph-based methods.

4.2 Connectivity map learning strategy

In this section we propose a learning strategy based on TSP, aimed to recover the overall link signals of a wireless communication network from the observation of signals observed over a subset of sampled links.

Before describing the methods developed within Task 3.1, we recall some basic concepts of topology, starting from graphs, only for the sake of clarifying the successive TSP tools. As well known, a graph is a simple example of a topological space. In particular, a graph $G(\mathcal{V},\mathcal{E})$ is composed of a set of elements (vertices) $\mathcal{V}$ and a set of edges $\mathcal{E}$ representing pairwise relations among data. However, graph-based representations are not always able to capture all the complex interactions among the constitutive elements of interconnected systems that cannot be reduced to pairwise relations, but require multiway descriptors.

The direct extension of a graph, involving higher-order interaction forms, is a simplicial complex [MUN18]. A simplicial complex $\mathcal{X}$ is composed of an ensemble of vertices $\mathcal{V}$ and an ensemble $\mathcal{S}$ of subsets of vertices, called *simplices*. A simplex of order k, or k-simplex, is a set of $k+1$ vertices denoted as $\sigma_i^k \equiv \{v_{i_0}, v_{i_1}, \dots, v_{i_k}\}$. A *face* of a k-simplex is a $(k-1)$-simplex of the form $\{v_{i_0}, \dots, v_{i_{j-1}}, v_{i_{j+1}}, \dots, v_{i_k}\}$, for some $0 \le j \le k$. Every k-simplex has exactly $k+1$ faces. The defining property of a simplicial complex $\mathcal{X}$ is that it is a finite collection of simplices that is closed under inclusion of faces, i.e., if $\sigma_i \in \mathcal{X}$, then all faces of σ_i also belong to $\mathcal{X}$. Then, for example, a vertex is a 0-dimensional simplex, an edge is a simplex of dimension 1, a triangle is a simplex of dimension 2. The dimension (or order) of a simplex is one less than its cardinality. The dimension of the simplicial complex is the largest dimension of any of its simplices. An example of simplicial complex of order 2 is illustrated in Figure 16, including the triangle $\{v_1, v_2, v_3\}$.

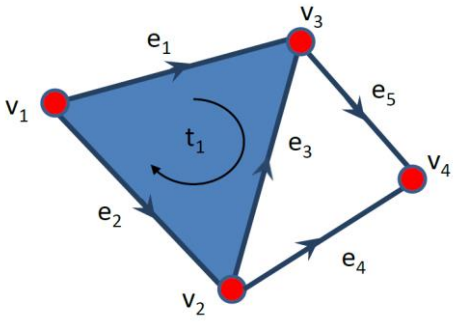

Figure 16: Example of simplicial complex of order 2.

The structure of a simplicial complex $\mathcal{X}$ of order K, is fully described by the set of its incidence matrices $\mathbf{B}_k$ of order k, with $k = 1, \dots, K$. The entries of the incidence matrix $\mathbf{B}_k$ establish which k-simplices are incident to which $(k-1)$-simplices. If we wish to represent, for example, a simplicial complex of order two, composed of a set $\mathcal{V}$ of vertices, a set $\mathcal{E}$ of edges, and a set $\mathcal{T}$ of triangles, having cardinalities $V = |\mathcal{V}|$, $S = |\mathcal{E}|$, $T = |\mathcal{T}|$, respectively, we need two incidence matrices: $\mathbf{B}_1 \in R^{V \times E}$ and $\mathbf{B}_2 \in R^{E \times T}$.

The connectivity properties of a simplicial complex of order K are fully captured by its high-order combinatorial Laplacian matrices of order $k = 0, \dots, K$, defined as $\mathbf{L}_k = \mathbf{B}_k^T\mathbf{B}_k + \mathbf{B}_{k+1}\mathbf{B}_{k+1}^T$ where $\mathbf{L}_k^{low} = \mathbf{B}_k^T\mathbf{B}_k$ and $\mathbf{L}_k^{up} = \mathbf{B}_{k+1}\mathbf{B}_{k+1}^T$ are the lower and upper Laplacian matrices expressing, respectively, the lower and upper adjacency of k-order simplices. So, for example, two edges are lower adjacent if they share a common vertex, whereas they are upper adjacent if they are faces of a common triangle. An interesting property of the incidence matrices is that $\mathbf{B}_k\mathbf{B}_{k+1} = \mathbf{0}$, for all $k = 1, \dots, K-1$. This property induces a decomposition of the signal subspaces associated with simplicial complexes complexes of various order, known as Hodge decomposition [MUN18], that in the case of a simplicial complex of order 2 is written as

$$R^E \equiv \mathrm{img}(\mathbf{B}_1^T) \oplus \ker(\mathbf{L}_1) \oplus \mathrm{img}(\mathbf{B}_2)$$

where the kernel of $\mathbf{L}_1$ is called the harmonic space. As explained in [BAR20], a signal defined over the edges of a network can be well represented as a linear combination of the eigenvectors of $\mathbf{L}_1$, which can be subdivided in three qualitatively distinct classes: the vectors lying in the nullspace of $\mathbf{L}_1$; the eigenvectors associated with the nonzero eigenvalues of $\mathbf{B}_1^T\mathbf{B}_1$; the eigenvectors associated with the nonzero eigenvalues of $\mathbf{B}_2\mathbf{B}_2^T$.

From Hodge decomposition, an edge signal $\mathbf{s}^1$ can always be expressed as the sum of three orthogonal components:

$$\mathbf{s}^1 = \mathbf{B}_1^T\mathbf{s}^0 + \mathbf{s}_H^1 + \mathbf{B}_2\mathbf{s}^2$$

representing, respectively, the solenoidal (i.e., divergence-free) component $\mathbf{s}_{sol}^1 = \mathbf{B}_2\mathbf{s}^2$, the irrotational (curl-free) component $\mathbf{s}_{irr}^1 = \mathbf{B}_1^T\mathbf{s}^0$, and the harmonic flow $\mathbf{s}_H^1$. This represents the discrete counterpart of the the decomposition of a vector field.

4.2.1 Learning strategy

In this section we recall the learning strategy developed in [BAR20] used to recover the overall link signals of a wireless communication network from the observation of a subset of sampled signals. The proposed method consists of the following three steps:

1) Infer the simplicial complex from the observed edge signals;
2) Find a sparse representation of the edge signals;
3) Use sampling theory over simplicial complexes to recover the entire edge signals from the observation of the signals over a subset of edges.

We start from the topology of the network, which represents the underlying graph, i.e. a simplicial complex of order 1. Then, we proceed to infer the presence of triangles, i.e. a complex of order 2 from the observation of a set of M edge (flow) signals $\mathbf{X}^1 = [\mathbf{x}^1(1), \dots, \mathbf{x}^1(M)]$. Since the graph is given, $\mathbf{B}_1$ is known, hence we only need to infer the structure of $\mathbf{B}_2$. Since the only signal components that depend on $\mathbf{B}_2$ are the solenoidal and harmonic components, we need first to check whether the observed signals have such components. To do that, we project the observed flow signal vector onto the space orthogonal to the space spanned by the irrotational component, by computing

$$\mathbf{x}_{sH}^1(m) = \left(\mathbf{I} - \mathbf{U}_{irr}\mathbf{U}_{irr}^T\right)\mathbf{x}^1(m), \quad m = 1, \dots, M$$

where $\mathbf{U}_{irr}$ is the matrix whose columns are the eigenvectors associated with the nonzero eigenvalues of $\mathbf{B}_1^T\mathbf{B}_1$. If the sum of the square norms of $\mathbf{x}_{sH}^1(m), \quad m = 1, \dots, M$, exceeds a given threshold η, then we proceed to estimate $\mathbf{B}_2$.

Then, considering all cliques of three elements present in the graph, the matrix $\mathbf{B}_2\mathbf{B}_2^T$ can be written as $\mathbf{B}_2\mathbf{B}_2^T = \sum_{n=1}^{T} t_n \mathbf{b_n}\mathbf{b_n^T}$ where t_n is a binary coefficient and $\mathbf{b_n}$ is the vector of size E

associated with the n-th clique, whose entries are all zero except the three entries associated with the three edges of the n-th clique. We find the binary coefficients t_n by using the minimum total variation (MTV) algorithm proposed in [BAR20], which aims at minimizing the total variation of the observed edge signals over a simplicial complex of order 2. Then we solve the following problem

$$\begin{aligned} \min_{\boldsymbol{t}\in\{0,1\}^T} \quad & q(t) \equiv \sum_{n=1}^{T} t_n \, trace(\mathbf{X}_{SH}^{1\,T} \mathbf{b}_{\boldsymbol{n}} \mathbf{b}_{\boldsymbol{n}}^{\boldsymbol{T}} \mathbf{X}_{SH}^{1}) \\ s.t. \quad & \|\mathbf{t}\|_0 = t^*, t_n \in \{0,1\}, \forall n \end{aligned}$$

where t^* is the number of triangles that we aim to detect. In practice, t^* is not known, so it has to be found through cross-validation. Interestingly, even though the above problem is non-convex, for any given t^*, it can be solved in closed form.

After learning the simplicial complex structure, for any observed vector $\mathbf{x}^1(m)$, we look for sparse representations of the observed flows by estimating the sparse vector $\mathbf{s}^1$ that solves the following basis pursuit problem:

$$\begin{aligned} \min_{\mathbf{s}^1\in R^E} \quad & \|\mathbf{s}^1\|_1 \qquad (\mathcal{P}_s) \\ s.t. \quad & \|\mathbf{x}^1 - \mathbf{V}\mathbf{s}^1\|_F \leq \epsilon \end{aligned}$$

where the dictionary $\mathbf{V}$ is the eigenvector matrix of $\mathbf{L}_1 = \mathbf{B}_1^T\mathbf{B}_1 + \mathbf{B}_2\mathbf{B}_2^T$, with $\mathbf{B}_2$ estimated with our data-driven inference method.

The sparse signal representation obtained solving problem $\mathcal{P}_s$ enables the use of the sampling theory so that we can retrieve the entire edge signal from the observations over a subset of edges. We say that the edge signal $\mathbf{s}^1$is $\mathcal{F}$-bandlimited if it can be written as $\mathbf{s}^1 = \mathbf{V}_{\mathcal{F}}\mathbf{s}^1_{\mathcal{F}}$ where $\mathbf{V}_{\mathcal{F}}$ is the $E \times |\mathcal{F}|$ matrix whose columns are the eigenvectors of $\mathbf{L}_1$ associated with the frequency index set $\mathcal{F}$ and $\mathbf{s}^1_{\mathcal{F}}$ is a vector of coefficients, named graph Fourier transform coefficients, of size $|\mathcal{F}|$. Exploiting the bandlimited property of the edge signals and then the sampling theory, we use the following recovery rule [BAR20] to retrieve the overall flow signal from the samples:

$$\mathbf{s}^1 = \mathbf{U}_{\mathcal{F}}(\mathbf{U}_{\mathcal{F}}^T\mathbf{D}_{\mathcal{S}}\mathbf{U}_{\mathcal{F}})^{-1}\mathbf{U}_{\mathcal{F}}^T\mathbf{s}^1_{\mathcal{S}}$$

where $\boldsymbol{D}_{\mathcal{S}}$ is a edge limiting operator, i.e. a diagonal matrix whose i-th entry is equal to 1 if the edge $e_i \in \mathcal{S}$ and zero otherwise.

4.2.2 Numerical results

We tested our algorithm over a wireless communication network modelling the data traffic among N=20 transceivers located on the area of the city of Rome, nearby the School of Engineering of Sapienza University of Rome, as illustrated in Figure 17.

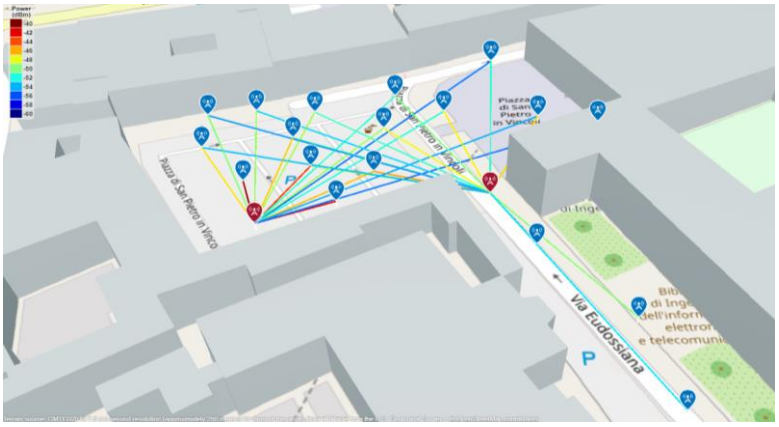

Figure 17: An example of observed link signals

We considered two possible transmitters, represented by the two red dots, and then a set of 20 possible receivers, represented by the blue dots. For each transmit/receive (Tx/Rx) pair, we measured the RSS at the receiver, using a ray-tracing tool. In the example reported in the above figure, the RSS is represented by the color over each edge (the scale goes from yellow color that represent high values to blue colors that represent low values). From the RSS, we derive the spectral efficiency using Shannon formula. In this way, we have a set of data rates, one for each edge reported in Figure 17. The goal of our processing is to infer the structure of a simplicial complex from these measurements to be able to apply the sampling theory described before. From the matrix of the observed edge signals, we infer first the presence of triangles of the simplicial complex of order 2 by using the Minimum Total Variation Algorithm (MTV). Then we apply the sampling theory to predict the values of the data rates over unobserved Tx/Rx pairs. To test the goodness of the propose strategy, we compared the proposed strategy with a conventional graph-based approach. To perform the comparison, we report the Mean Square Error (MSE) as a function of the number of observed (edge) signals, i.e. data rates.

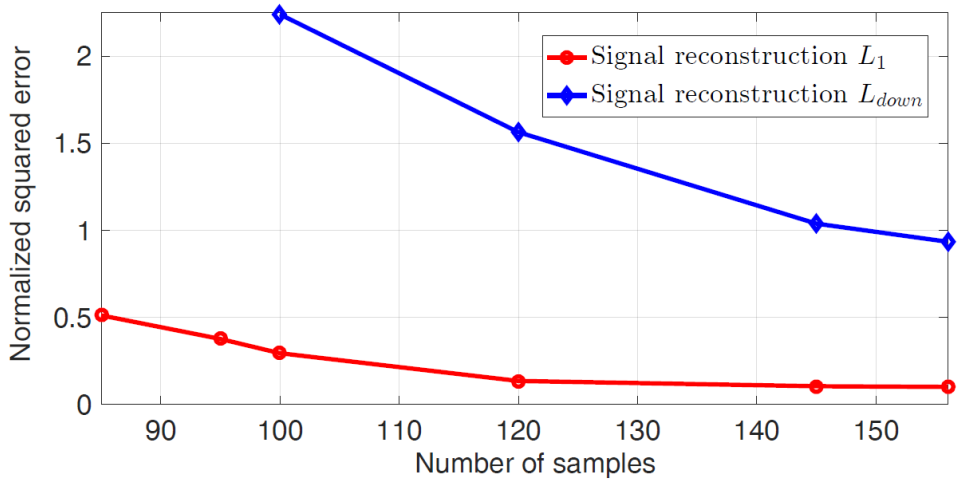

Figure 18: Normalized squared error versus number of samples

In Figure 18 we report the normalized squared error versus the number of samples used to recover the signals, obtained using the proposed approach (red curve) and a conventional graph-based approach. It can be noted from Figure 18 that, for any number of samples, we can achieve a much smaller error by using a simplicial complex based approach. The reason

of this improvement is due to the capability of the simplicial complex representation to better capture the relations between signals defined over the edges of a network.
While in this first part of the activities of WP3 we used measurements obtained from a ray-tracing tool running in an urban environment, the goal of our current work is to apply the developed algorithms to analyze data provided by ITRI inside the IMTC industrial facility to test the capability of the proposed methods in an industrial environment.

5 Service placement and request routing

One of the most important issues to tackle network planning is the placement of network services in Edge Servers (ES), and the routing of applications requested by the end users (sensors, machines, etc.) with low latency requirements, exploiting storage and computing resources at the edge, which are typically limited with respect to the central cloud.

5.1 State of the art

In the MEC paradigm, resource-intensive and delay-sensitive applications are offered directly from edge clouds, to exploit the potentials of cloud computing without incurring in high latency links to communicate with remote core clouds. But of course, the computation and storage capabilities of the edge cloud are much more limited than those available in a cloud data center. To overcome this issue, virtualization techniques such as virtual machines (VMs) and containers can help in creating an open edge computing environment, in which the edge nodes inside a common geographical area form a cluster of shared resource. To fully exploit this edge cloud, we need to optimize resource placement and scheduling, i.e. we need to find out optimal mechanisms to decide in which edge server to store analytic data necessary to run a requested application and where to offload and process data from querying devices. Most of the works in literature considers the allocation of communication, computation and caching resource separately or partially jointly. In particular, the research community exploits the joint allocation of computation and communication resource, as in [CHEYAO18], whose target is to minimize the delay for offloading tasks in a Software Defined Network. In [DEH17], the authors investigate the problem of developing optimal joint routing and caching policies in a network supporting in-network caching with the goal of minimizing expected content-access delay, proposing a greedy solution based on sub-modularity properties. Caching and computation resource are jointly optimized in [TUY19] decomposing the original problem into a cache placement problem and a video request scheduling problem aiming at minimizing the expected delay cost of video retrieval. Recently, the authors in [DRA18] proposed a joint optimization problem for scaling, placing, and routing services described as templates in the network, and containing information about the components of the network services. Each flow is then routed through a network path, after adding or removing services to dynamically handle the workload changes. Only few works have considered together communication, computation and caching resource. In [HEKHA18], the authors solve the problem of service placement and request scheduling leveraging sub-modularity properties and an approximation algorithm. The considered edge cloud system aims to maximize the number of serving requests, allowing direct access only to one server per user, while edge nodes are connected via backhaul links to share services. The work in [POU20] is the most similar to the one we have developed for Task 3.2, which we are presenting here. In [POU20], they consider overlapping coverage areas for edge nodes with the aim to minimize the request routing to the core cloud (to maximize the assignment at the edge). The problem of service placement and request routing is handled with constraints on computation, caching and communication capacities, through an approximation algorithm for randomize rounding the real solution, inspired by [ARA1999]. Their algorithm may violate storage constraints and the problem is tackled iteratively removing services in edge nodes and then redirect correspondent requests.

5.2 Proposed method

We consider a wireless edge network consisting of a set $\mathcal{N}$ of edge nodes, each one endowed with a MEC server to enable virtualizing network services/applications (VNFs), i.e. equipped with storage, computation and communication capabilities.

We assume that there is a set $\mathcal{S}$ of network services, usually consisting of virtual machines (VMs) and/or containers, able to run such sophisticated applications. The services can be

stored on the edge clouds in order to satisfy a set $\mathcal{K}$ of user devices (UDs), each demanding for network services. Each edge node n, with $n \in \{1,2,\dots,N\}$, is assumed to be endowed with a wireless access point, covering local areas, possibly overlapping, over which are distributed the user devices, subscribers of the MEC operator. Without loss of generality, each device $k \in \{1,2,\dots,K\}$, is supposed to request only one service $s \in \{1,2,\dots,S\}$, whereas the same user generating multiple requests will be modeled as multiple devices, possibly requesting different network applications. The system receives requests from users in a stochastic manner, and are supposed to be predictable for a certain time interval. The offered network services can be identified by three parameters, regardless the specific querying UD:

- b_s : the amount of data offloaded by the device to enable the service
- ω_s : the amount of CPU cycles needed to process the task
- m_s : the amount of memory required to store data at the server, in order to run the application.

For each device k, we define a subset $\mathcal{N}_k$ of edge servers such that a connection can be established between the device and this group of nodes. It is a neighbourhood clustering consisting of edge nodes within a distance $d_{kn} < d_{th}$, allowing a request to be routed to a server, closer then a predefined threshold d_{th} and storing the correspondent data. If none of the neighbour edge nodes cached the demanded service, the device can be routed to a data center, generically indicated as a *core cloud* C_L, storing the entire set S of services. Of course, if this happens, it would not be without incurring in a higher cost in terms of communication latency, being the core cloud at a much longer distance with respect to all the other nodes in the edge cloud. We consider two types of resource constraints at the edge nodes: *computation limits,* due to the maximum computational capacity of the server available to run a given amount of information units; *storage limits,* due to the maximum storage capacity of the server available to cache a limited amount of information units. To find out the decision rule about where to store network services and where to serve user requests, we leverage two sets of binary optimization variables:

$\mathbf{x} = (x_{sn} \in \{0,1\} : s \in \mathcal{S}, n \in \mathcal{N})$**:** placing service s in node ,

$\mathbf{y} = (y_{kn} \in \{0,1\} : k \in \mathcal{K}, n \in \mathcal{N})$**:** routing device k to node .

The aim of our approach is to minimize the total latency occurred for receiving a service, i.e. the delay for transmitting data from a device to an edge cloud, and the delay introduced by the selected server to run the requested application.

Communication delay

We suppose that the channel state information (CSI) is perfectly known at the transmitter as well as at the receiver sides. The transmission rate depends only on the path-loss attenuation experienced by the channel h_{kn} , along the communication link between the serving node n and the requesting device k. Using Shannon formula, we compute the capacity of the link between the user device k and the edge server n as:

$$R_{kn} = B\ log_2\left(1 + \frac{Ph_{kn}}{N_0 B}\right) \qquad (1)$$

where N_0 in the noise power spectral density, B is the bandwidth and P is the transmission power. In this work, we consider an homogeneous network in which all user devices have the same maximum transmit power and the same portion on the total frequency band. We suppose that the radio access point can apply an orthogonal multiple access technique to serve all assigned devices, to avoid interference. In this case, each user has the same chance to transmit at its own maximum possibilities, given the channel h_{kn}. Thus, the *radio* delay component depends only on the amount of data b_s^k that each device k wants to offload to the edge node n , in order to enable the desired service s:

$$\mathcal{L}_{kn}^R = \frac{b_s^k}{R_{kn}}. \qquad (2)$$

Processing delay

Each edge-cloud node can slice its computation capacity to serve different types of service requests. We consider an equal portion f_{kn} of the CPU capacity allocated by each server n to process any task s required by user k. The CPU architectures are supposed to be similar on each edge node, in order to have the same performance for running a virtual machine (or a container). Thus, the time spent to process the received data and then to run an application, depends only on the amount of workload ω_s^k that the application itself requires to be processed by the edge server, for device k :

$$\mathcal{L}_{kn}^C = \frac{\omega_s^k}{f_{kn}}. \qquad (3)$$

In particular, the workload ω_s can be regarded as the amount of CPU cycles a specific application s requires to run, and it is computed as: b_s/J_s, where J_s indicates how many bits per CPU cycle have to be processed from the given application.

5.3 Problem Formulation

The target of our optimization problem is to find the optimal service placement allowing all user devices to obtain the requested services in the shortest possible time, including routing the requests to the optimal edge node. The objective of our problem is then to minimize the total delay experienced by each user device when routed to a serving node. This implies the minimization of the sum of communication and computation delays, as previously defined, to upload and then process the data at the selected edge cloud.

Integer Linear Programming formulation

The optimization problem can be formulated as follows:

$$
\begin{aligned}
\min_{\mathbf{x},\mathbf{y}} \quad & \sum_{k=1}^{K}\sum_{n=1}^{N} y_{kn}\left(\frac{b_s^k}{R_{kn}}+\frac{\omega_s^k}{f_{kn}}\right) \\
subject\ to \quad & a)\ \sum_{n\in\mathcal{N}_k\cup\{C_L\}} y_{kn}=1, \qquad \forall k\in\mathcal{K} \\
& b)\ y_{kn}=0, \qquad \forall k\in\mathcal{K}, n\notin\mathcal{N}_k \\
& c)\ y_{kn}\le x_{s^k n}, \qquad \forall k\in\mathcal{K}, n\in\mathcal{N} \\
& d)\ \sum_{s=1}^{S} x_{sn}\, m_s\le M_n, \qquad \forall n\in\mathcal{N} \\
& e)\ \sum_{k=1}^{K} y_{kn}\, f_n\le F_n, \qquad \forall n\in\mathcal{N} \\
& f)\ x_{sn}\in\{0,1\}, \qquad \forall n\in\mathcal{N}, s\in\mathcal{S} \\
& g)\ y_{kn}\in\{0,1\}, \qquad \forall n\in\mathcal{N}\cup\{C_L\}, k\in\mathcal{K}
\end{aligned}
\qquad (\mathcal{P}) \qquad (4)
$$

where the objective function is the total delay, whereas constraint (a) ensures that a user device is routed, in order to be served, only to one of its neighbouring edge clouds or to the core cloud; constraint (b) ensures that a device can be served only if connected to a server; constraint (c) states that a device's request is routed only to edge nodes already storing that service; constraint (d) ensures that a node can store data in terms of bytes as much as its maximum capacity allows, and finally constraint (e) ensures that a server can split its processing capacity in a limited number of slices simultaneously. These capacity constraints lead the algorithm to balance storage and computation resources, although this is not the direct target of the problem. This comes as a consequence of network services virtualization, that reduces the *cost* of caching data in terms of reserved Gigabytes, by sharing the same virtual machines (and/or containers) between querying devices, regardless of the individual requirements b_s and ω_s.

Approximation Algorithm

Constraints (f) and (g) show the binary nature of problem $\mathcal{P}$, which is inherently combinatorial and usually very difficult to handle, especially in scenarios where many devices are involved. To tackle this computational issue, we first relax the problem by letting the variables x_{sn} and y_{kn} to be real, within the interval $[0,1]$, i.e., by changing the last constraints in problem $\mathcal{P}$ as:

$$
\begin{aligned}
& f)\ \ x_{sn}\in[0,1] \qquad && \forall n\in\mathcal{N}, s\in\mathcal{S}, \\
& g)\ \ y_{kn}\in[0,1] \qquad && \forall n\in\mathcal{N}\cup\{C_L\}, k\in\mathcal{K}.
\end{aligned}
\qquad (5)
$$

Then, we run a Linear Program solver to obtain a very fast real-valued solution and apply a randomized routing method. This technique, as suggested in [Tul20], allows us to round the relaxed solution and obtain integer values, with provably approximation guarantees. Using real placement variables $\hat{x}_{sn}$, the new integer values $\tilde{x}_{sn}$ are set equal to 1 with probability $\hat{x}_{sn}$. Then, after checking for each service where it has been stored, the algorithm routes a device to only one corresponding edge node with probability $\hat{y}_{kn}$, i.e. there is a probability $\hat{y}_{kn}$ to

choose one node within all nodes caching the service requested by a device, and if the new variable value is $\tilde{y}_{kn} = 1$ that n is the only picked server node. The requests are routed to the core cloud in only two cases: after the first random rounding, if none of the edge server cached the requested service; after the second rounding if none of the edge servers is picked to serve a device. It can be proved that the solution of the proposed approximation algorithm satisfies in expectation the storage and the computation constraints. Thus, we repeat the rounding procedure many times to exploit the redundancy of the probabilities and prove the bounds, such that only feasible solutions are considered for the expectation.

5.4 Matching algorithm

To prove the effectiveness of the proposed algorithm, we evaluate the performance comparing the results with those obtainable using a *matching theory* algorithm. Matching theory studies the problem of associating agents belonging to two different sets using suitable preference lists. Typical matching problems are stable marriages and college admission procedures [Gale62], where students apply to colleges based on their preference lists and are accepted based on colleges' preference lists. While marriages pertain to *one-to-one* matching, the college admission problem is a *many-to-one* matching, where multiple agents from one set (the students) can be assigned to one agent of the other set (a college). Typically, each college cannot accept more students than a given threshold, otherwise the matching problem would be trivial and just based on students' preferences. defined as its quota q. The aim of matching theory algorithms is to find a *stable* assignment. An assignment of applicants to colleges is called *unstable* if there are two applicants α and β who are assigned to colleges A and B, respectively, although β prefers A to B and A prefers β to α. A matching is stable if it is not unstable. Matching theory has been extensively used in economics and recently it has been introduced in wireless networks [Han17].

In the C-RAN context, the authors in [Li17] find an assignment of UE's to Radio Remote Head (RRH), Base Band Unit (BBU) and computing resources to minimize the refusal ratio, i.e. the portion of requests that cannot meet their deadlines. The preference function is based on the *expected* delay that a user would experience choosing a certain triple RRH, BBU, and computing resource. In [Merl19], the authors propose a dynamic computation offloading algorithm to jointly optimize computation and communication resources and mobile users assignment to APs and edge servers, merging tools from stochastic optimization and matching theory. In [Gale62], the Deferred Acceptance (DA) algorithm is presented and proved to converge to a stable matching. In the DA algorithm, students apply to their preferred college, which subsequently accept students in a waiting list, based on their preference, rejecting the least preferred ones. Then, the rejected students apply to their second choice. At this point, the colleges again accept the most preferred students, rejecting the others (possibly also the ones already present in their waiting lists). The process stops when all the students are assigned to one college, or no students apply to any college. Inspired by this procedure, we propose an algorithm where the APs are the colleges and the users (i.e. the services) are the students. Each AP has a certain quota, which is defined differently from the previous example. Indeed, since APs have limited computing and storage capacities. In particular, we denote by M_n the storage capacity of AP n, and by C_n its computing capacity. Then, an AP n can accept users until both M_n and C_n are not saturated. Thus, the quota is not defined by a number of users, but it depends on the accepted services and it is directly linked to the computing and storage capacities of the AP.

5.5 Numerical Results

All simulations are performed in Matlab® environment. We considered three types of virtual machines [Zak21] as possible service network requests: micro, small and extra large, each type having its own requirements in terms of processing and storage. The values of CPU cycles necessary to run the services varies from 500 to 2000MHz and the memory involved varies from 0.6 to 3.7 GB. The data arrivals offloaded by the sensors are generated with a Poisson distribution with mean arrival rate uniformly distributed within [0.4, 1.1] Mbps. The popularity profile for $S = 400$ service requests is derived from the Zipf distribution with shape parameter 0.8, that is a typical value for several network services. There are $K = 400$ devices, uniformly distributed in an area 700m x 500m, which offload their data to five possible edge nodes $N = 5$. The equal bandwidth portion assigned to each device to access the edge cloud is $B = 10$ MHz, the carrier frequency is $f_c = 28$GHz, and we assume a Rayleigh fading channel with unit variance. The noise spectral density is $N_0 = -174$dBm/Hz, and the maximum transmit power of the querying devices is $P = 100$mW, used to compute the maximum achievable data rate.

We compare the proposed algorithm, denoted as RR, with two other methods:

- *Linear-Relaxation (LR)*: the real solution of our original problem;
- *Matching Algorithm (M)*: a Matching-based algorithm, as described in the previous section.

LR is the initial solution of our algorithm, although there is no physical meaning in routing a portion of a request, it can be regarded as a benchmark, a lower bound to measure how far from the optimal is the integer solution provided by our algorithm.

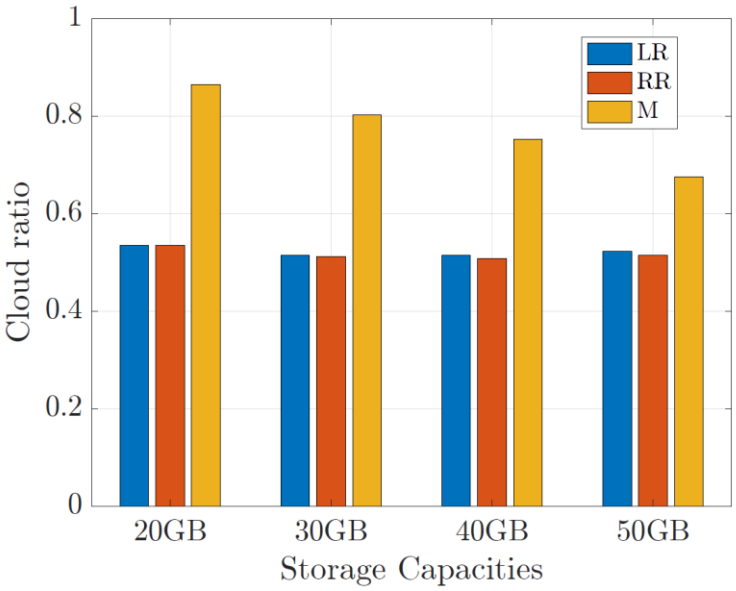

Figure 19: Quote of assignments to core cloud

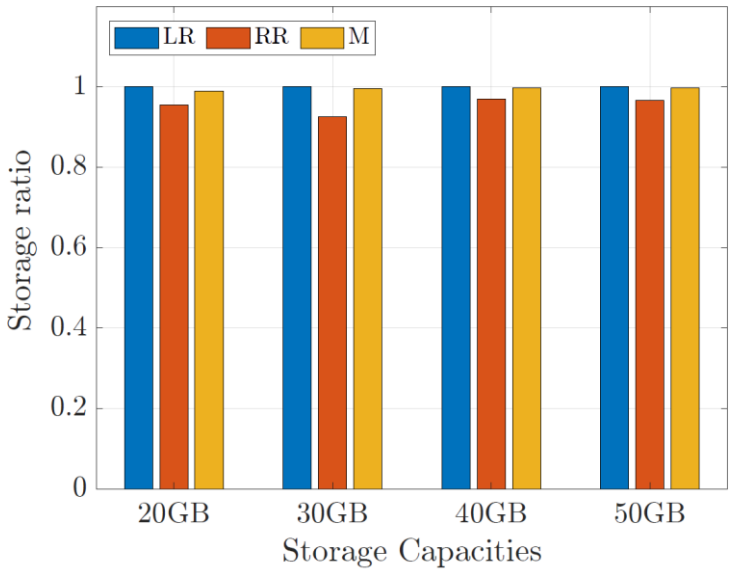

Figure 20: Amount of storage involved in the service placement

We first explore the impact of different values of the storage capacity M_n, considering the sum of all edge nodes. In Figure 19, report the cloud ratio, defined as the sum of all the requests routed to the core cloud C_L with respect to the total number of requests arrived from all user devices, as a function of the storage capacity. From Figure 19, we can see how the proposed algorithm (*RR*) provides performance very close to the optimal (*LR*) solution and it decides to offload to remote cloud less requests with respect to the matching algorithm (M). . In Figure 20, we show the storage ratio, defined as the amount of memory involved to run all the applications over the edge servers, with respect to their maximum capacity, supposed to be the same for all the serving nodes. We first notice that the capacity size does not impact the service placement decision. From the point of view of the matching algorithm, this is due to the scarce overall capacity. On the other hand, our solution copies the requested services as much is possible through the edge cloud with the aim of minimizing the delay in delivering these applications once required, as there is no cost to store the data in our current formulation. In future developments, we plan to incorporate penalties to prevent an excessive use of copying, thus saving memory occupation.

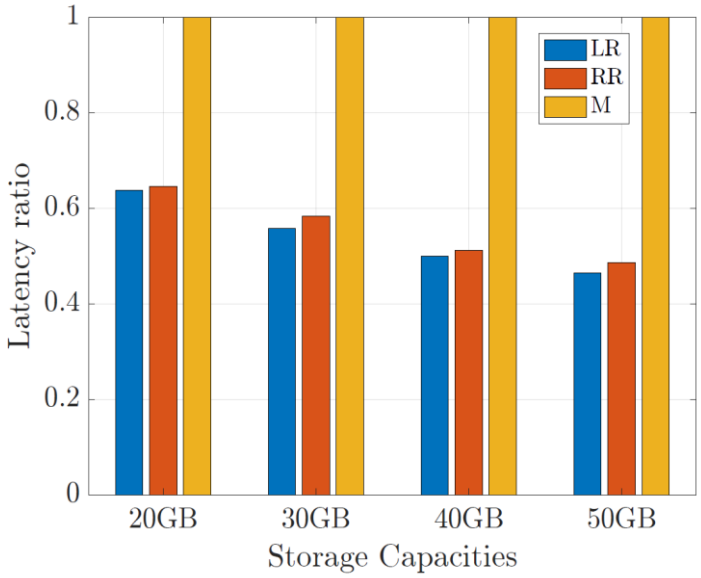

Figure 21: Total latency experienced respect to the maximum value

In Figure 21 we report the ratio between the total latency experienced using our proposed algorithms and the total latency achievable with optimal matching theory, as a function of the storage capacity of each storing device. The result is very clear: the proposed method clearly outperforms the matching algorithm: furthermore, it is evident how the more storage capacity is available at each server, the less requests are routed to the core cloud, and then the system experiences less delay in delivering the results from the applications. The matching algorithm experiences a bigger delay due to a frequent request routing to the central cloud, especially when the bound on the storage capacity is very tight. Our algorithm performs much better because the service placement allows the system to amortize the cost of storing a lot of data, reusing the same virtual machine for more users. Of course, this can be done for shareable resources as for analytic data cached at the server, otherwise computation and communication resources need to be dedicated to the specific querying devices.

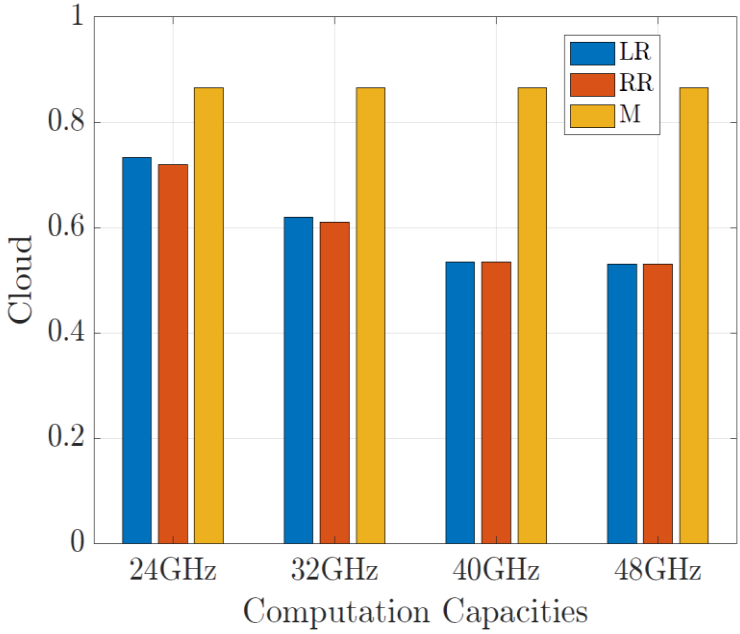

Figure 22: Quote of assignments to core cloud

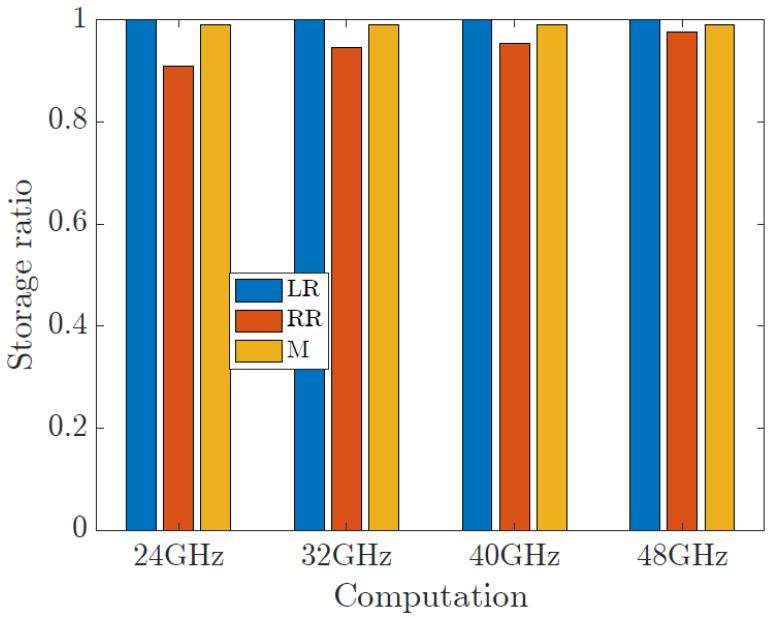

Figure 23: Amount of storage involved in the service placement

Next, we consider the impact of computation capacity at the edge nodes. Figure 22-Figure 24 show how different bounds on the computation capacities constraint impact on the performance of the service placement and request routing paradigm. Our approximation algorithm, based on the random rounding of a real linear solution, leverages the increasing in CPU frequency available at the edge servers to route the requests to AP nodes rather than to the remote cloud. Of course, this comes with a benefit in the total latency experienced by the system, even if less than the benefit experienced with more storage capacity. The matching theory algorithm, based on the best SNR association, does not take any advantage, again because the allocated resources are the minimum possible to satisfy as much as it can all the requests. At the same time, this solution is not aware of the placement and thus cannot amortize the size of the storage already occupied to run the same services. For delay-sensitive services, it is very important to be served within the edge cloud and the proposed algorithm satisfies the request for such applications in a very fast and efficient way.

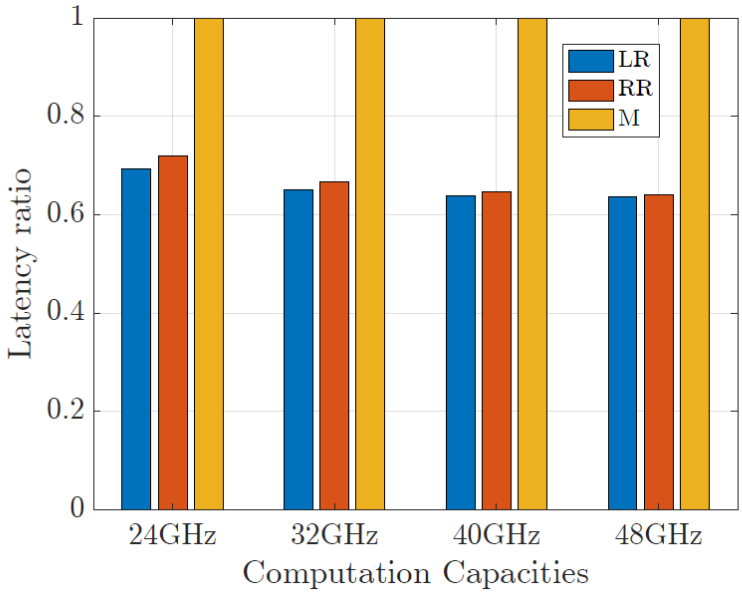

Figure 24: Total latency experienced respect to the maximum value

6 Capacity dimensioning and optimal placement of radio access and sensing nodes

This section is dealing with the planning of private 5G radio networks designed for the industrial use cases identified in Work Package 1. The objective is to accurately predict the shop floor indoor wireless network performance prior to installation. This could help the network designer to assess the number and location of base stations that we should deploy to ensure the target requirements of vertical applications will be met.

6.1 State of the art

The cell planning relies on different types of tools to aid the radio planner with the process. These tools enable accurate prediction and verification of radio coverage and quality. Ranplan is one of the main commercial tools that can support the planning process from end to end, which covers the following key features:

- 3D modelling of buildings and outdoor environments: Based on the floor plan in different formats, such as DWG and PDF imported to Ranplan, the perfect 3D modelling of the building can be rapidly created and displayed.
- Coverage prediction and service outage identification: A deterministic 3D ray launching and tracing radio propagation model has been integrated to Ranplan. The signal is radiated from the antenna and converted to rays in all directions, then they transmit freely in the surrounding space until they encounter an obstacle. The model is able to estimate the indoor, outdoor, indoor to outdoor(leakage) or outdoor to indoor(ingress) RF coverage. Three-dimensional predictions can be performed and analyzed for all frequency bands and displayed on the actual floor plan in terms of different performance metrics, such as path loss, best server, Signal-to-Interference-plus-Noise Ratio (SINR) and throughput. The predictions of RF signal are essential for the radio designer to appreciate the coverage they can expect in the building and avoid any possible service-outage area. In addition, using the Intelligent Cell Optimization (ICO) module, the location and transmit power of base stations can be optimized to achieve the required performance indicators.
- Wireless network simulator: Ranplan is equipped with a sophisticated wireless network simulator that can emulate different traffic profiles of the use case by populating the network with a set of user equipment using a mix of vertical services. The system level simulation shows how real-life network performance varies under different scenarios and helps the RF engineer identify areas that need to be improved.

In the following sections, Ranplan professional v6.4 will be adopted as the toolkit for the indoor radio planning at IMTC.

6.2 Building Structure and Antenna Modeling

When predicting the signal coverage and quality, the materials and respective scales associated with the building are taken into account to provide very accurate results. To this end, the 3D building structure modeling of the trial site IMTC has been conducted to form the basis for the accurate calculation of radio propagation prediction via ray tracing. As shown in Figure 25 and Figure 26, the stations for the machining process are distributed across the whole shop floor with about 2000 square meters large. Various material of walls and surfaces including glass, plaster, coated glass, metal and plastic are incorporated in the 3D building model. The Ranplan contains the material database to define as closely as possible the building characteristics and environment. In the following sections, the indoor radio planning will be performed within the demonstration area where the use cases described in D1.1 are implemented, as seen in Figure 27. It consists of two CNC stations and a cloud-based controller for fixture system with vibration mitigation.

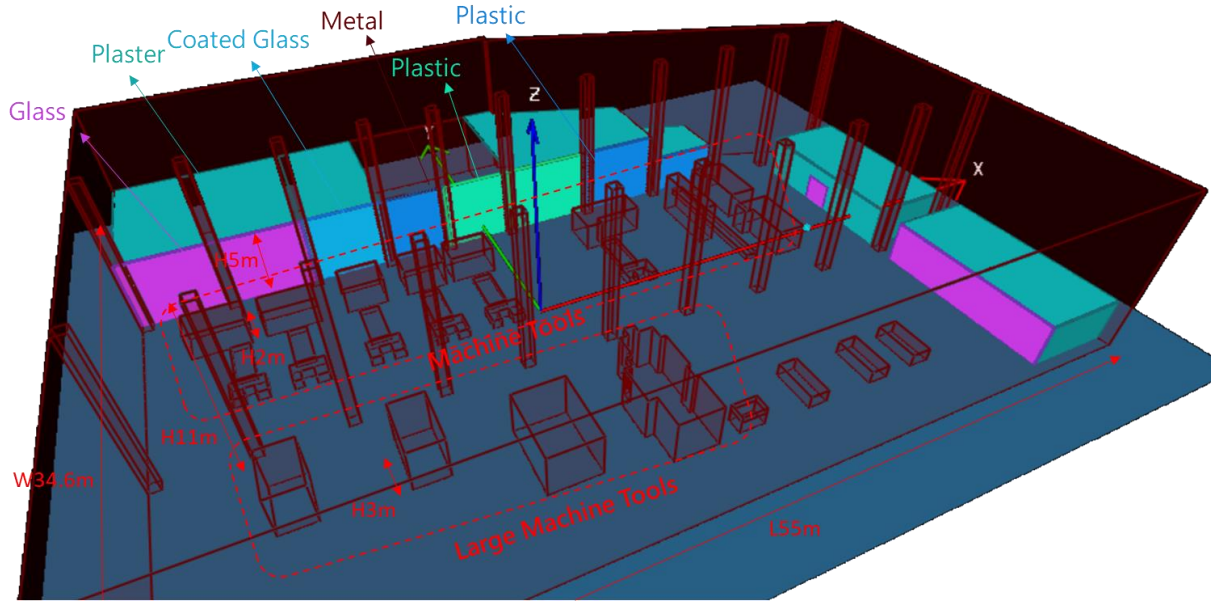

Figure 25: IMTC Building Structure Modeling

Figure 26: IMTC shop floor

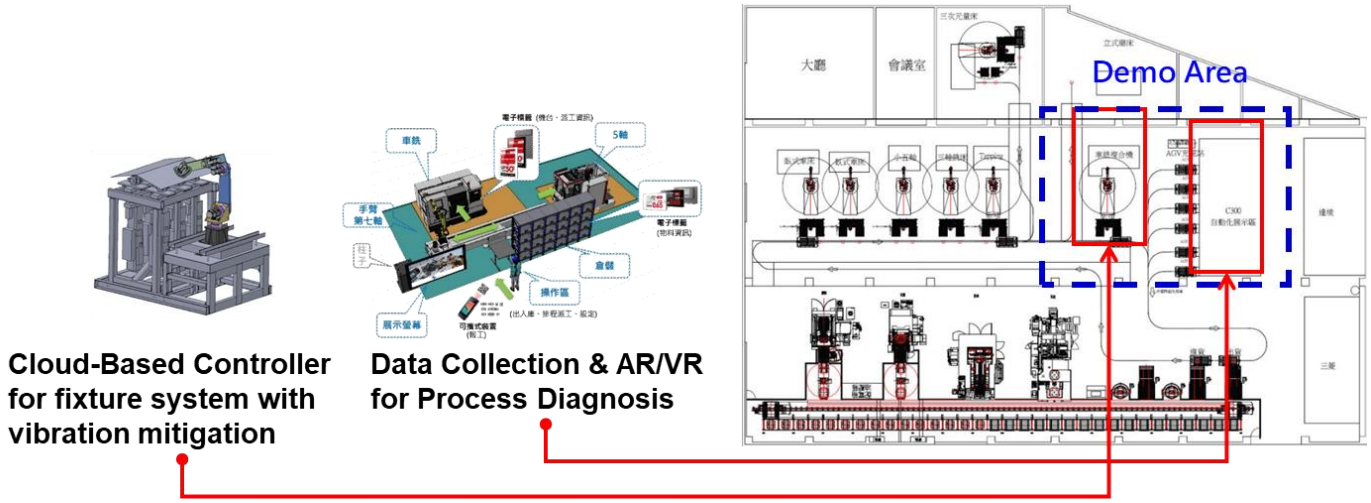

Figure 27: IMTC floor plan and the vertical applications

In addition, 4x4 MIMO antenna patterns of the gNB supplied by Alpha Networks have been measured and imported to the device database. The two-dimensional horizontal and vertical patterns for antenna 1 are shown in Figure 28. Based on the XYZ coordinate system, the horizontal pattern refers to the data on the XOY plane, 0-359 degree, starting from positive X axis and vertical pattern refers to the data on the XOZ plane, 0-359 degree, starting from positive X axis. The 90 and 270 degree represent the ground and ceiling respectively in vertical pattern. Finally, the 3D antenna pattern will be generated based on these inputs using interpolation techniques.

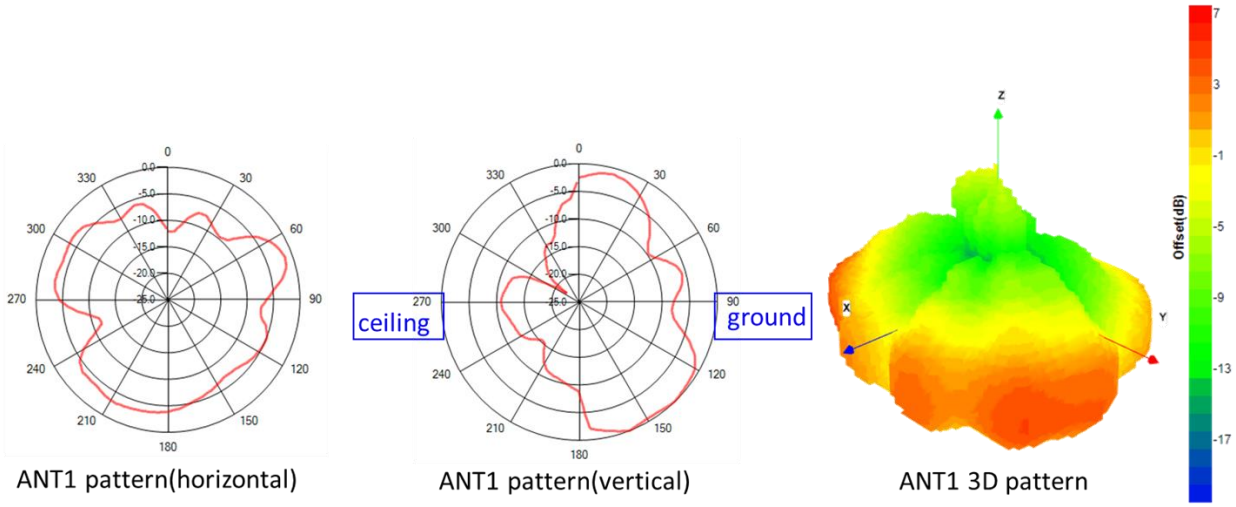

Figure 28: 2D and 3D antenna pattern for antenna 1 of the RU

6.3 Coverage and Key Performance Metric Analysis

One essential part of the indoor radio planning is to evaluate the coverage through two main network parameters, namely SS-RSRP and CSI-SINR. They will be elaborated first and followed by the predicted results.

When the mobile switch is on, it will perform the cell selection procedure to select a suitable cell with sufficiently high received signal power. To this end, the mobile will measure the synchronization signal reference signal received power (SS-RSRP), which is the average power per resource element carrying cell's Secondary Synchronization Signal (SSS) and check if the received signal power is high enough based on the cell selection criteria. If the criteria are not satisfied, the mobile device will not initiate the random-access procedure to contact the base station and of course will be unable to register with the 5G network. In addition, when the mobile is in the state of RRC_IDLE and moves away from the serving base station, it will again measure the SS-RSRP of serving and neighboring cells and decide if reselect to a better cell based on the cell reselection criteria. Finally, SS-RSRP is one of the measured quantities used for handover procedures. As described above, SS-RSRP is one of the critical factors for coverage evaluation.

The above analysis reveals the signal strength and coverage of the serving cell but the interference is not taken into account. The CSI-SINR (Channel State Information-Signal to Interference plus Noise Ratio) is measured on the CSI-RS (Channel State Information Reference Signal) and will not only reflect the signal strength but also the signal quality. With link adaptation scheduling, the base station is switching dynamically between different Modulation scheme and Coding Schemes (MCS) based on the UE-reported CQI (Channel Quality Indicator). The CQI is derived by the UE and mainly depends on the CSI-SINR. It describes the state of the downlink radio channel and indicates the fastest MCS that the UE can handle with a certain BLER (Block Error Ratio). As an illustrative example, Figure 29 shows that the base station uses 256-QAM or 64-QAM at high CSI-SINR to give a high data rate, but falls back to 16-QAM or QPSK at lower CSI-SINR to reduce the number of errors. Since two base stations with the same frequency are deployed in this example, the UE at the cell edge will encounter heavy interference and has poor CSI-SINR values.

MCS index	Modulation Order	DL Throughput (Mbps, theoretical value)	DL Throughput (Mbps, simulation value)	CSI-SINR
0	2	48	31~201	0.61~11.4
1	2	76		
2	2	122		
3	2	178		
4	2	239		
5	4	300	328~528	12.2~17.8
6	4	344		
7	4	388		
8	4	438		
9	4	488		
10	4	522		
11	6	554	634~998	19~38
12	6	615		
13	6	674		
14	6	732		
15	6	792		
16	6	855		
17	6	918		
18	6	977		
19	6	1038	1009~1442	39~47.48
20	8	1082		
21	8	1127		
22	8	1195		
23	8	1263		
24	8	1333		
25	8	1403		
26	8	1453		
27	8	1503		

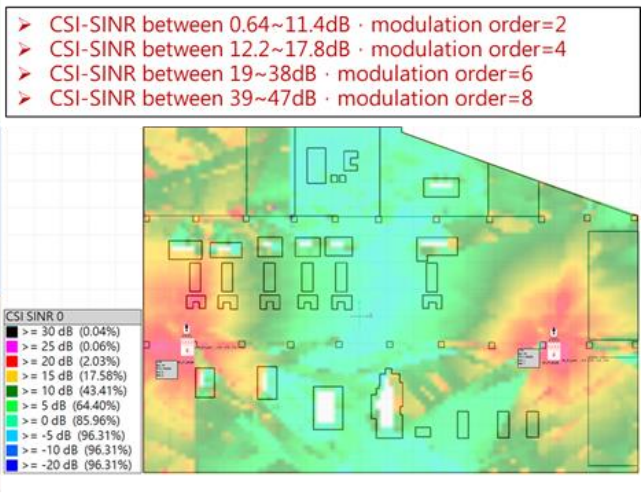

Figure 29: Downlink Throughput Simulation at Different Channel Conditions

Based on the 3D building structure and antenna model from section 6.2, the predicted results for SS-RSRP and CSI-SINR are provided in Figure 30. The proportion of SS-RSRP value over -90Bm is virtually 100%. In the meantime, full coverage with CSI-SINR above 30dB can be achieved. It is important to note that the simulation results here only reveal the signal strength

or quality at a certain location. Traffic requirements of vertical applications will be incorporated in the next section.

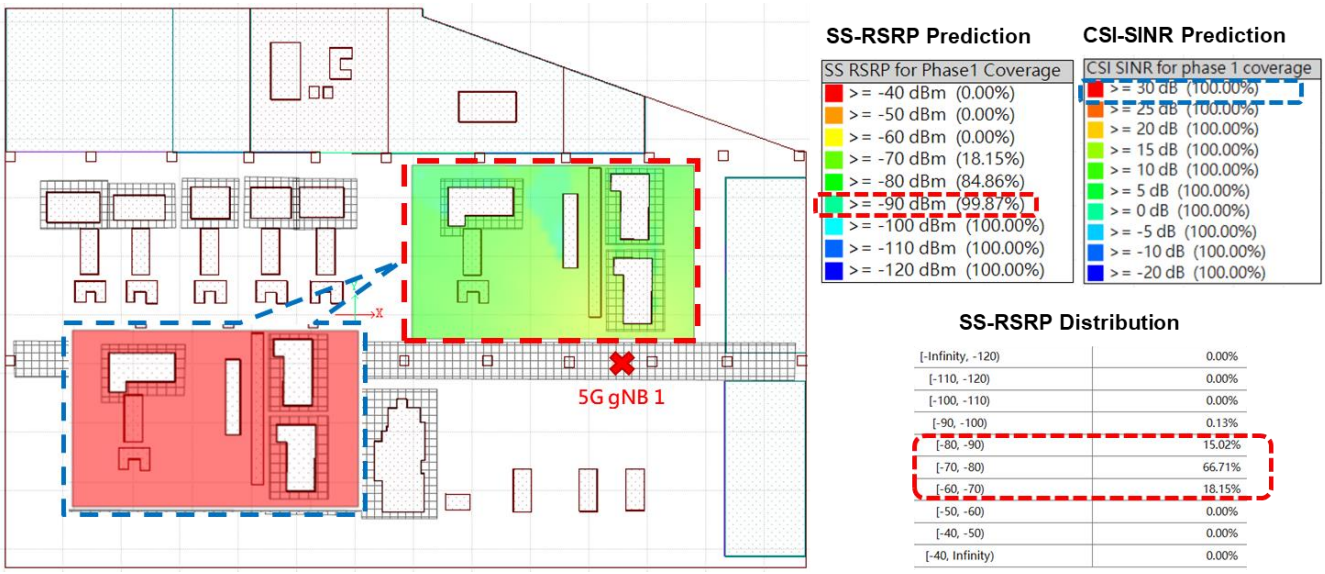

Figure 30: SS-RSRP and CSI-SINR predictions

6.4 System Performance Evaluation of Real-life Network Deployment

The prediction results in section 6.3 ensure the basic connectivity of a mobile with certain signal strength or quality requirements. In this section, we're going further to incorporate the traffic map of vertical use cases in order to evaluate the performance of real-life network deployment. In particular, Figure 31 illustrates the traffic map that specifies the traffic characteristics and traffic service area. Three use cases described in D1.1 are planned to be implemented and installed in the same factory and served by the same 5G system, namely UC1: Process diagnostics by CNC and sensing data collection, UC2: Using Augmented/Virtual Reality for Process Diagnosis and UC3: Cloud-Based Controller for fixture system with vibration mitigation. The QoS requirements for each use case are provided, which includes downlink throughput, uplink throughput, number of users and mobility. The CPEs for UC1 and UC3 are considered to be fixed in the green and blue region respectively, while the AR users for UC2 are expected to move slowly in the green region.

Use Cases	Mobility	Num. of users	UL TPut requirement	DL TPut requirement
Process Diagnostics by CNC and Sensing Data Collection	Fixed (green region)	2 CPEs	CNC & sensing data:16Mbps/UE	NA
Augmented/Virtual Reality for Process Diagnosis	Pedestrian (green region)	2 AR glasses	Live video: 2Mbps/UE	Remote rendering data: 50Mbps/UE
Cloud-based Controller for fixture system with vibration mitigation	Fixed (blue region)	1 CPE	<1 Mbps/UE	<1 Mbps/UE

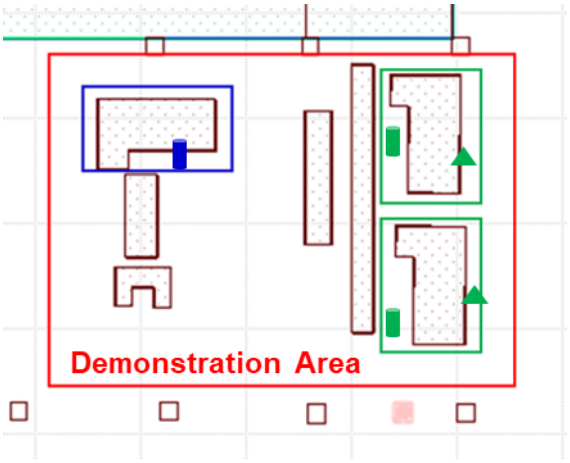

Figure 31: Traffic Map of Three Use Cases

In addition, some important scheduling parameters of the base station that will influence the user experience are taken into account and collected in

Table 2. In particular, the TDD UL-DL configuration defines the uplink/downlink allocation in the time domain with D representing a downlink-only slot, U representing an uplink-only slot and S representing a switching slot. The switching slot begins with 10 downlink symbols, continues with two flexible symbols used as guard period and ends with two uplink symbols. Since the combined use cases require data transfer in both downlink and uplink directions, the pattern of DSUUDDSUUD will be used in the simulation. The downlink MIMO transmission supports Open-Loop Spatial Multiplexing (OLSM) with up to 4 different streams of traffic while the uplink MIMO transmission supports diversity processing with a single stream of traffic.

Table 2: Key scheduling parameters of the base station

Parameters	**Value**
Center Frequency	4850MHz
Channel Bandwidth	100MHz
gNB max Tx power	24dBm
Downlink MIMO mode	OLSM(4x4)
Uplink MIMO mode	Diversity

TDD UL-DL config.	DSUUDDSUUD
TDD switching slot config.	D10G2U2
Max DL/UL Modulation	64QAM/64QAM
Scheduling algorithm	proportional fair

The objective is that the throughput requirements of each user should be met while the cell load (time-frequency resources of the base station) is less than 90% to account for fluctuations of traffic. Figure 32 illustrates aggregated UE positions of 1000 snapshots of the simulation using Monte-Carlo style population of the network. One of the snapshots is shown in Figure 33 and each user is associated with a table of predicted uplink and downlink performance metrics including RSRP, SINR, CQI, throughput, etc.

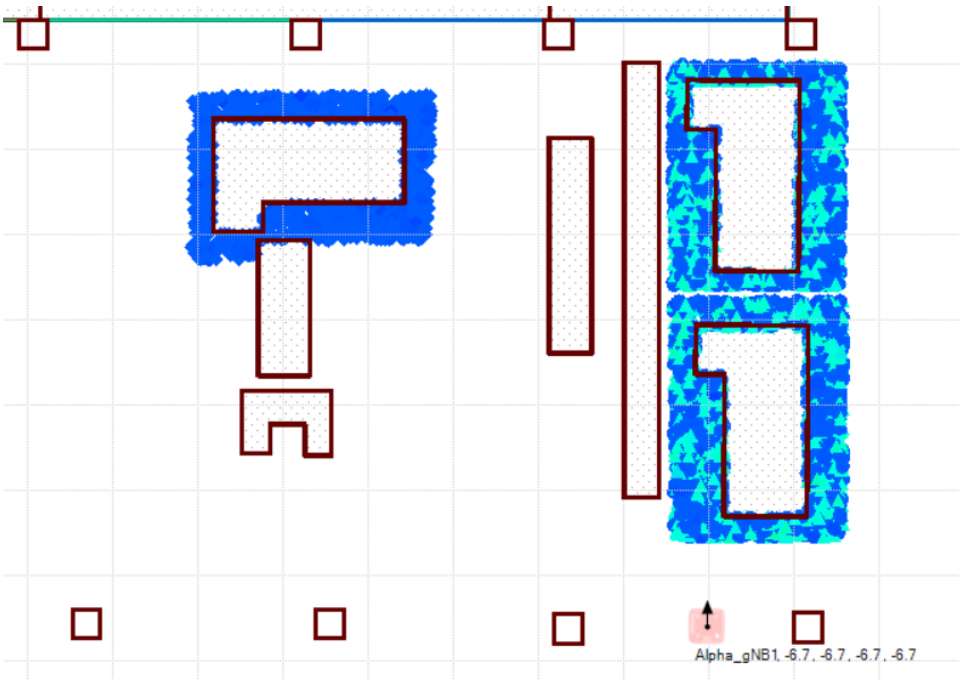

Figure 32: Combined UE Positions of 1000 Snapshots of Simulation

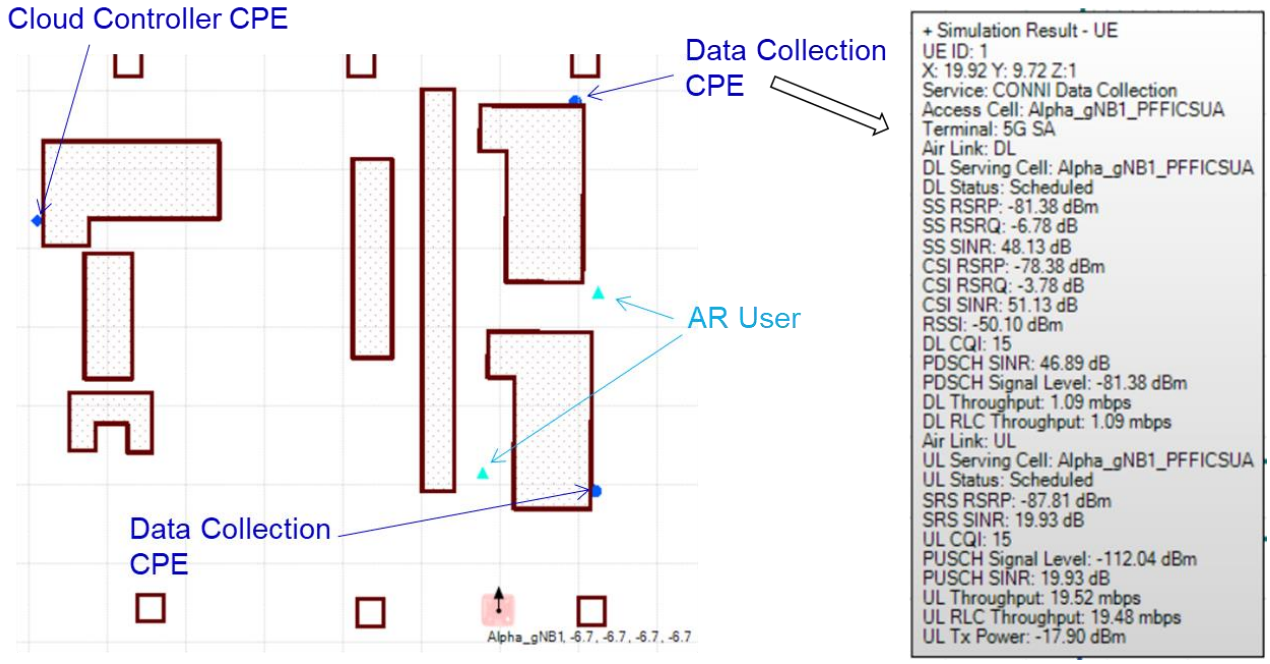

Figure 33: One Snapshot of System Performance Simulation

The simulation result is provided in Table 3 and it shows that the network design is expected to meet the target requirements of the use cases in the specified area. The predicted average downlink and uplink throughput per UE for UC1 are 1.1 and 19.508 Mbps respectively, 56.387 and 3.74 Mbps for UC2, and finally 1.096 and 1.904 Mbps for UC3. Moreover, the downlink and uplink cell load are 8.5% and 20.2% respectively, which is far below the 90% threshold. This is in line with our expectations since the demonstration area is small and has virtually uniform channel conditions with SINR above 30dB. The number of UEs that provide wireless connectivity might be subject to changes in the coming months, based on the actual implementation described in D5.2.

Table 3: System Performance Simulation Results

Traffic Results	**User DL Avg. TPut (Mbps)**	**User UL Avg. TPut (Mbps)**	**DL Cell Load**	**UL Cell Load**
2 data collection CPEs	1.1	19.508 (>16)	8.5%	20.2%
2 AR users	56.387 (>50)	3.74 (>2)		
1 cloud controller CPE	1.096 (>1)	1.904 (>1)		

7 Preliminary considerations for network monitoring performance

The private 5G system in 5G-CONNI project consists of RAN including CPE, MEC and 5G core. In order to check if the system meets the design criteria and have a better knowledge of how the 5G system performs, each of the network components will monitor the corresponding KPI.

The section will include the following subtasks:

- RAN monitoring
- Core network monitoring
- Edge cloud monitoring

7.1 RAN monitoring

The picture reported below shows the network architecture of this 5G-CONNI project in Taiwan side. To fulfill the requirements of the use cases, which were described by the consortium in D1.1, some KPIs need to be considered in the RAN side and E2E system. In this chapter, KPIs in RAN will be addressed.

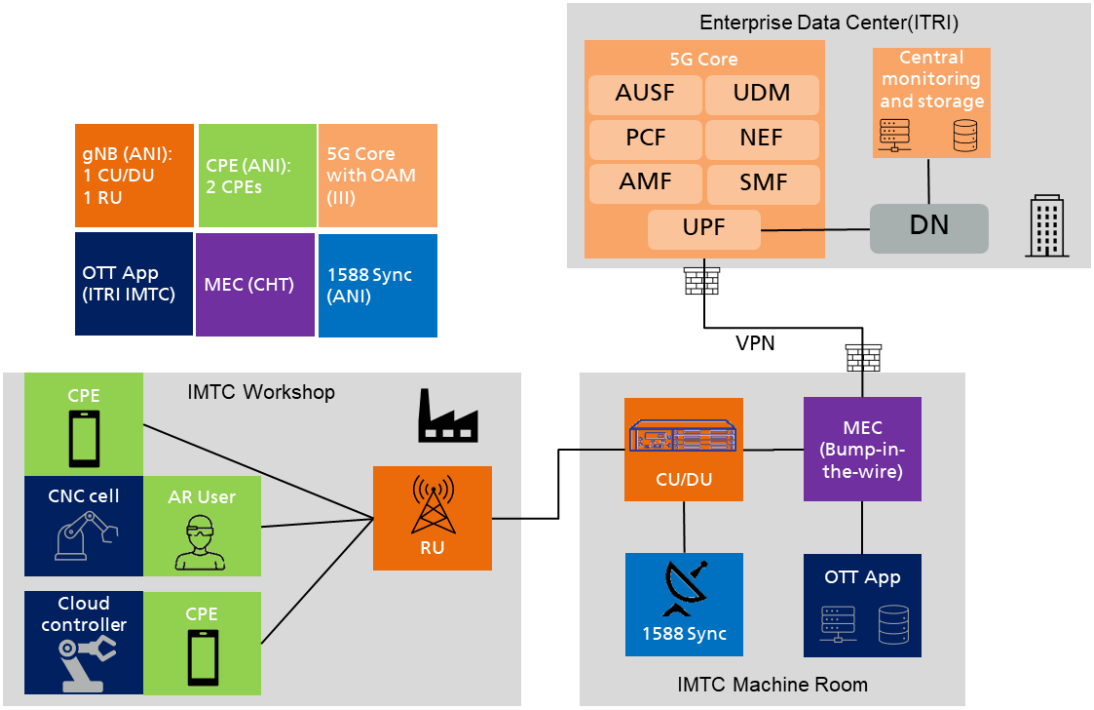

Figure 34: Network Architecture in Taiwan side.

7.1.1 State of the art

In the RU and CU/DU, e.g. RAN, the specification of M-Plane form O-RAN Alliance monitoring/management architecture is considered to be implemented. The protocol of NETCONF server will be used in the RU and CU/DU in order to connect to the NETCONF client in NMS which is embedded in the same server of 5G Core provided by III. YANG model for RU and CU/DU will be the interfaces between RAN and NMS.

In the O-RAN Alliance, the only RU parameters, which have to be managed, are defined in [YANG21]. This is not sufficient for monitoring the system in IIoT application. Alpha Networks will define the required parameters to fulfill the purpose of CM, FM and PM. All the monitored parameters will be sent to NMS with the NETCONF protocol and vice versa, NMS can configure RAN as well.

7.1.2 KPI of throughput, latency and reliability [ANI] 14-07

From Figure 34, there are three use cases (UC-1, UC-2, and UC-3 in D1.1) will be implemented at ITRI IMTC, The KPI will be designed accordingly. Basically, for UC-2: Using Augmented/Virtual Reality for Process Diagnosis, downlink throughput maybe the key indication. Downlink

latency between *MEC and RU* may also be considered to be monitored. For UC-3: Robot Platform with Edge Intelligence and Control, the monitoring of UL parameters, e.g. throughput and latency are addressed.

System reliability is also a key performance indicator. Considering the maintenance, parameters related to system reliability need not only to be monitored but also to be configured.

7.2 Core network monitoring

The 5G Core Network Manager (CNM) was introduced to provide a single clean, consistent management interface regardless of network element type. The graphical interface was introduced to reduce training requirements, and allow operator personnel to quickly drill down to the source of any issue to keep your network running at optimal efficiency.

5G CNM consolidates OA&M operations for all network elements and provides:

- Fault Management of all network elements to provide best-in-class GUI capabilities by integrating with OAM
- Simple graphical datafill editor for Configuration Management
- Consolidated Performance Management of all network elements to provide simplified GUI with advanced features
- Robust Security Management to set user/group level controls to provide access to network elements

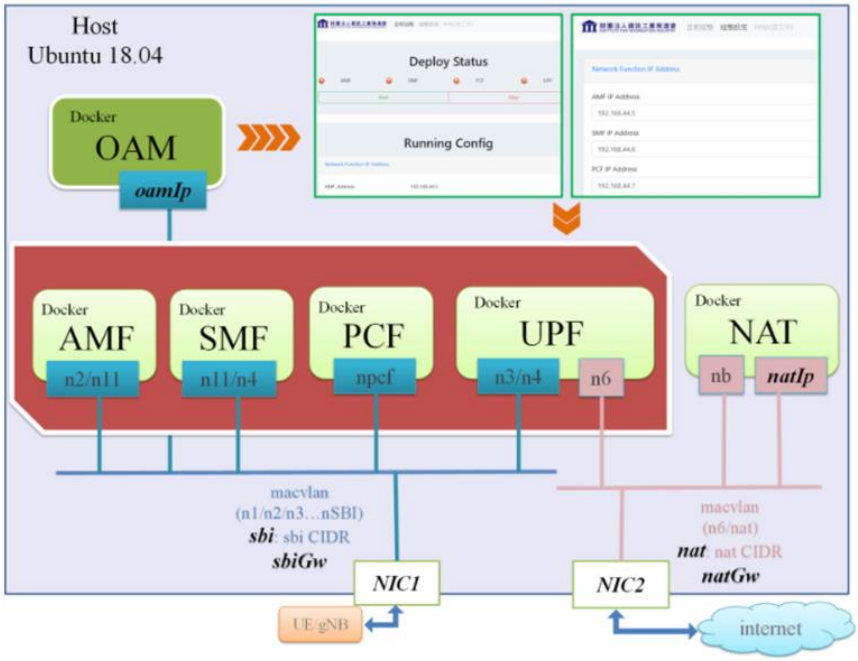

Figure 35: The Core Network Management architecture

A variety of changes are being implemented within 5G networks to meet efficiency, performance and unique demands of the various use cases, and the Operation Support Systems (OSS) require some fundamental changes as well. For the OAM Dashboard shown below, it uses the RESTful API and MQTT protocol to make the Fault Configuration Accounting Performance and Security (FCAPS) data available and integrated to CNM.

The figure below shows the Tabs of OAM Dashboard for general 5G Core execution information that includes the information like CPU Usage、Memory Usage and the healthy management of each PODs.

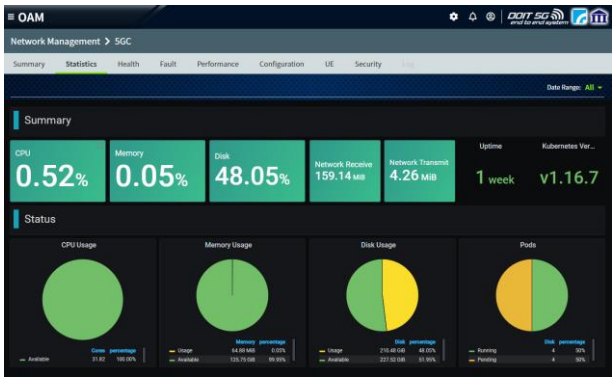

Figure 36: The general information of each 5GC module execution status.

For PM example, the performance management is dedicated to manage the overall performance of the network system and avoid the potential performance bottlenecks. In this part will collocate the system capacity intimations like count of connected gNBs registered UEs and established PDU sessions. Moreover, the data plane performance such as throughput and packets per second value can be seen in the following figure.

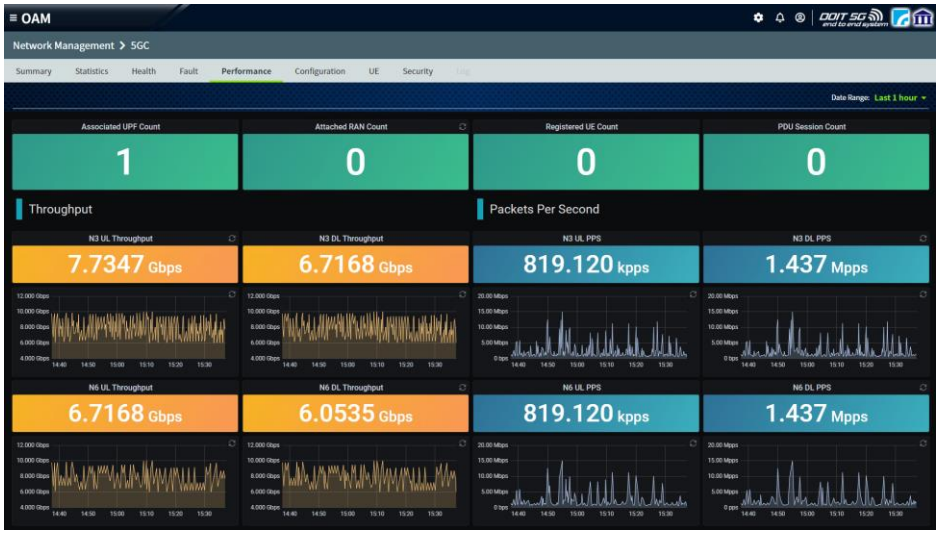

Figure 37: The PM of 5G Core OAM

7.3 Edge cloud monitoring

The edge cloud and MEC are the key elements in the private 5G network, which provide not only traffic steering functions but also the platform resources to deploy the industrial applications in the 5G CONNI project. The industrial applications must continue operation, so the monitoring of industrial applications is significant. The edge cloud and MEC can provide monitoring technologies. The following subsections describe the monitoring standard in the ETSI NFV group and the preliminary development of network monitoring.

7.3.1 State of the art

Monitoring VNF is essential for any NFV-like framework as the function maintains the performance and stability of VNFs for users. Moreover, ETSI NFV specifications have defined a monitoring architecture standard that specifies related interfaces and schemes to monitor various metrics of VNF. Therefore, implementing a flexible method for monitoring VNFs according to ETSI NFV specifications includes SOL 004 VNF package, SOL 003 VNF package management interface, SOL 002 VNF lifecycle management interface, and VNF Indicator interface. The VNF package contains the configuration parameters, monitoring methods, and resource information used to implement the VNF, which is managed through the VNF software package management interface to establish the resources of the VNF. After that, the VNF is created through the lifecycle management interface and monitored through the VNF indicator interface.

7.3.2 Preliminary development of network monitoring

The Taiwanese testbed monitoring method of 5G-CONNI includes four modules: registration, data collector, monitor, and event alert center. The combination of mentioned modules can provide users with a flexible monitoring VNF method from ETSI NFV specifications. First, the registration module implements the VNF package analysis function to analyze file formats and structures of SOL 004 that can specify the Indicator interface and metric type of VNF by using configuration files of the VNF package. After analyzing configuration files, the registration module can allocate resources and create virtual machines through NFVO/VNFM generated based on the architecture of SOL 003 and SOL 002. Furthermore, the registration module also uses the VNFM to inform EMs to monitor VNF metrics by the VNF Indicator interface implemented by the data collector module and the monitor module. The data collector module can obtain the specified metrics of the configuration file from VNFs, then the collector stores metrics in our database for checking the status of VNFs. Hence, the monitor module can retrieve each metric value of target VNFs from the database regularly, which maintains the performance and stability of VNFs for users. Once the metric value of databases is greater than the threshold of configuration files, the monitoring module will send an alert to our event alert center that can find suitable users to send alerts via SMS, email, or any connected alarm system.

In the Taiwanese testbed of the 5G-CONNI project, the MANO test environment is implemented based on ETSI standards for deploying our VNF monitoring method, as showed in Figure 38. The center of the Figure 38 illustrates the ETSI components and interfaces implemented, and the surrounding parts are monitoring modules:

1. The registration module can analyze indicator interface information and the metric type of the VNF packet specified in the Files folder by the users. The registration module registers interfaces and metrics with EM through VNFM, which actives the data collector module and monitor module to collect and retrieve metrics of specific VNFs.
2. Each metric of VNFs has a specified method to obtain data, which is defined in a customized metrics configuration and written into the files folder of the VNF package. Then collectors and monitors take VNF metrics according to specified methods (e.g., API, SNMP) from target modules, such as databases or VNFs.
3. Collectors and monitors regularly make examinations for metrics, and monitors also compare metric value between VNF and configuration files of the VNF package at the same time.
4. The event alarm centers for warning users are through emails, SMS when the VNF value is greater than the other. Users can receive detailed error information of the target VNF through the mobile phone or the user interface and perform related repair actions.

Using the registration, data collector, and monitor module, users can easily specify the VNF and resources to be monitored and observe metrics warnings on the user interface, as shown

in Figure 39. The user interface shows VNF alarms of the event center contained the event description, severity, time, and location for users to analyze problems of VNFs. 5G CONNI project has completed the deployment and monitoring of MEE VNF currently and will provide customized monitoring functions for upcoming ITRI applications in the future.

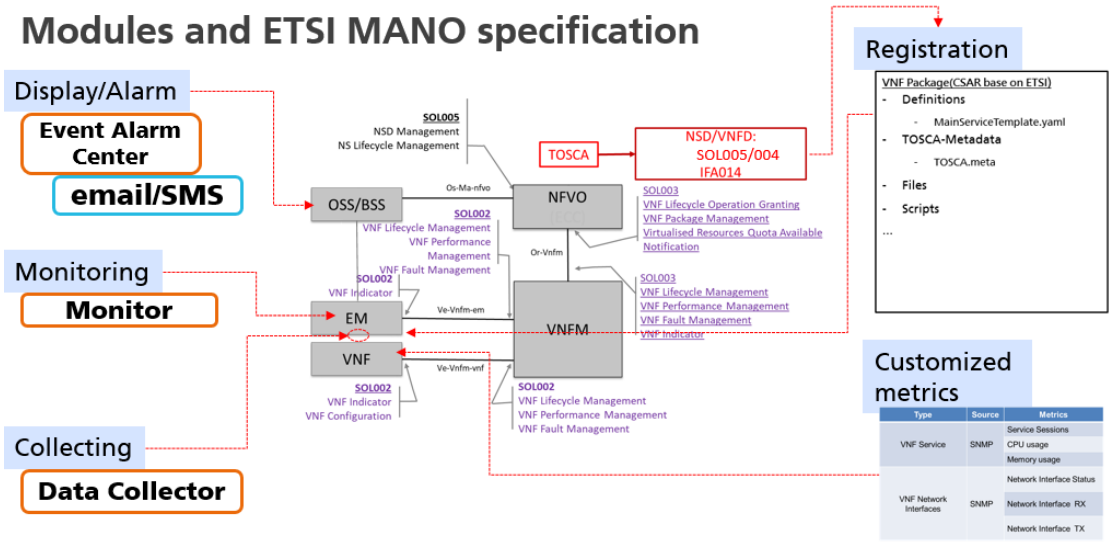

Figure 38: Modules and ETSI MANO specification

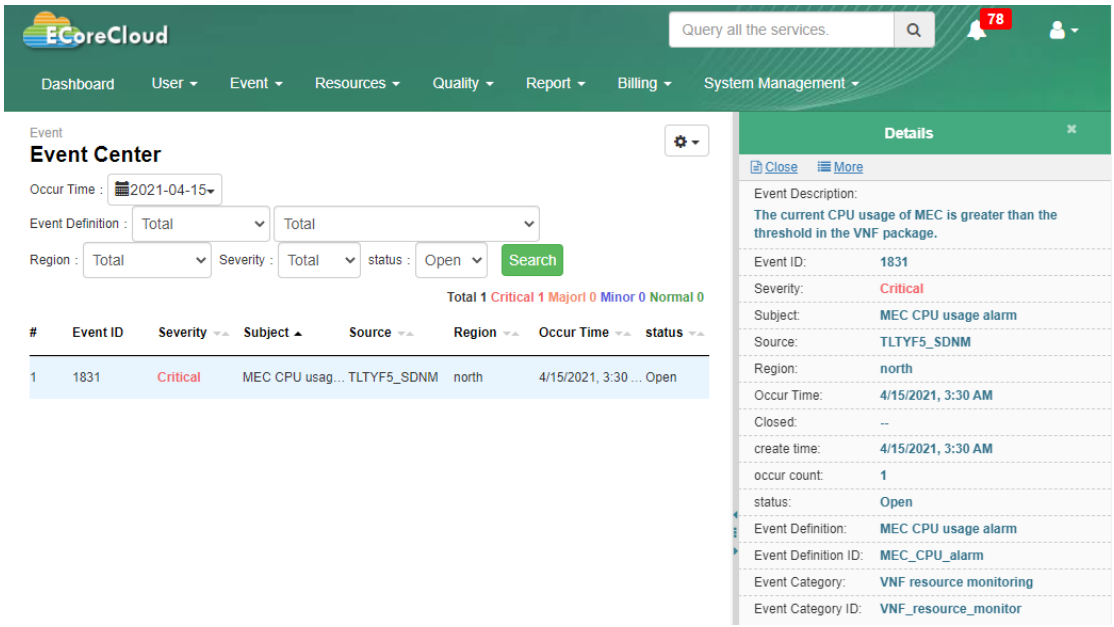

Figure 39: The user interface of monitoring event center

Taiwanese testbed monitoring method of 5G-CONNI has been developed. The next step is to choose one of the ITRI IMTC's applications to virtualize and network performance parameters of the industrial application to be monitored. All results will output in D3.2.

8 Conclusions

In this deliverable, we have presented the major results obtained in Tasks T3.1 and T3.2 of WP3. The channel sounder developed by HHI appears to be a very promising system to take channel measurements, able to measure not only power delay profile or delay spread, but also angular power distribution, which is a very interesting feature in MIMO systems. The measurement campaign carried out by HHI in a Bosch's facility has made possible to derive some preliminary channel models in the 3.7, 28 and 300 GHz bands. Further investigations will be carried out building on the real measurements collected in the measurement campaign. An algorithm for predicting a connectivity map from sparse measurements has been developed by SAP and tested over data obtained through ray-tracing tools. It is currently planned to perform a joint activity involving SAP and ITRI to test the algorithm over data provided by ITRI pertaining to the IMTC industrial facility. A further collaboration on this topic is planned with BOSCH researchers, whose goal is to infer, for example, a throughput map starting from RSS measures. An optimal algorithm has been developed by SAP to associate mobile devices to edge servers and allocate computational and caching resources in the edge cloud, in order to minimize the service delay, including communication and computation delays. Even though the original problem formulation entails a combinatorial search, which would be very problematic to handle when the number of devices increases, a sub-optimal method has been developed that is able to converge in a reasonable time and whose performance are in ay case better than a conventional matching algorithm.

The planning of private 5G radio networks designed for the industrial use cases identified in WP1 has also been carried out by ITRI and ANI, with the objective of predicting the performance of the indoor wireless network prior to installation. This analysis could be used by the network designer to assess the number and location of base stations that should be deployed to ensure that the target requirements of vertical applications will be met.

Finally, some preliminary considerations about how to monitor the network performance have been examined; including RAN monitoring (ANI), core network monitoring (III), and edge cloud monitoring (CHT). This activity will be further developed in the next months.

9 References

[AHN10] Y.-Y. Ahn, J. P. Bagrow, and S. Lehmann, “Link communities reveal multiscale complexity in networks,” Nature., vol. 466, pp. 761–764, 2010.

[ARA1999] Aravind Srinivasan. Approximation algorithms via randomized rounding: A survey. In Series in Advanced Topics in Mathematics, Polish Scientific Publishers PWN, pages 9–71. Publishers, 1999.

[BAR18] S. Barbarossa, S. Sardellitti, E. Ceci, M. Merluzzi, “The Edge Cloud: A Holistic View of Communication, Computation, and Caching”, Chapter 16 of Cooperative and Graph Signal Processing. Academic Press, 2018, pp. 419–444.

[BAR20] S. Barbarossa and S. Sardellitti, "Topological Signal Processing Over Simplicial Complexes," in IEEE Transactions on Signal Processing, vol. 68, pp. 2992-3007, 2020, doi: 10.1109/TSP.2020.2981920.

[BAR20_2] S. Barbarossa and S. Sardellitti, "Topological Signal Processing: Making Sense of Data Building on Multiway Relations," in IEEE Signal Processing Magazine, vol. 37, no. 6, pp. 174-183, Nov. 2020, doi: 10.1109/MSP.2020.3014067.

[BAZ11] J. A. Bazerque, G. Mateos and G. B. Giannakis, "Group-Lasso on Splines for Spectrum Cartography," in IEEE Transactions on Signal Processing, vol. 59, no. 10, pp. 4648-4663, Oct. 2011, doi: 10.1109/TSP.2011.2160858.

[BEN18] A. R. Benson, R. Abebe, M. T. Schaub, A. Jadbabaie, and J. Kleinberg, “Simplicial closure and higher-order link prediction,” Proc. of Nat. Acad. of Sci., vol. 115, no. 48, pp. E11221–E11230, 2018.

[CHE15] S. Chen, R. Varma, A. Sandryhaila and J. Kovačević, "Discrete Signal Processing on Graphs: Sampling Theory," in IEEE Transactions on Signal Processing, vol. 63, no. 24, pp. 6510-6523, Dec.15, 2015, doi: 10.1109/TSP.2015.2469645.

[CHEYAO18] M. Chen and Y. Hao. Task offloading for mobile edge computing in software defined ultra-dense network. IEEE Journal on Selected Areas in Communications, 36(3):587–597, 2018.

[DEH17] Mostafa Dehghan, Bo Jiang, Anand Seetharam, Ting He, Theodoros Salonidis, Jim Kurose, Don Towsley, and Ramesh Sitaraman. On the complexity of optimal request routing and content caching in heterogeneous cache networks. IEEE/ACM Transactions on Networking, 25(3):1635–1648, June 2017. Funding Information: National Science Foundation under Grant CNS-1413998 and Grant CNS-1117764. Publisher Copyright: © 2017 IEEE. Copyright: Copyright 2017 Elsevier B.V., All rights reserved.

[DIL18] P. Di Lorenzo, S. Barbarossa, P. Banelli, “Sampling and recovery of graph signals“, Chapter 9 of Cooperative and Graph Signal Processing. Academic Press, 2018, pp. 261-282.

[DRA18] S. Draxler, H. Karl, and Z. A. Mann. Jasper: Joint optimization of scaling, placement, and routing of virtual network services. IEEE Transactions on Network and Service Management, 15(3):946–960, 2018.

[EVA09] T. S. Evans and R. Lambiotte, “Line graphs, link partitions, and overlapping communities,” Phys. Rev. E, vol. 80, Jul. 2009, Art. no. 016105.

[FAR16] T. Farnham, "Radio environment map techniques and performance in the presence of errors," 2016 IEEE 27th Annual International Symposium on Personal, Indoor, and Mobile

Radio Communications (PIMRC), Valencia, Spain, 2016, pp. 1-6, doi: 10.1109/PIMRC.2016.7794911.

[GRA10] L. J. Grady and J. R. Polimeni, Discrete calculus: Applied analysis on graphs for computational science, Springer Science & Business Media, 2010.

[HAN19] Z. Han, J. Liao, Q. Qi , H. Sun, and J. Wang, “Radio Environment Map Construction by Kriging Algorithm Based on Mobile Crowd Sensing”, Hindawi, Special Issue on Secure Computation on 4G/5G Enabled Internet-of-Things, 2019.

[HEKHA18] T. He, H. Khamfroush, S. Wang, T. La Porta, and S. Stein. It’s hard to share: Joint service placement and request scheduling in edge clouds with sharable and non-sharable resources. In 2018 IEEE 38th International Conference on Distributed Computing Systems (ICDCS), pages 365–375, 2018.

[JIA19] J. Jia, M. T. Schaub, S. Segarra, and A. R. Benson, “Graph-based semisupervised & active learning for edge flows,” in Proc. 25th ACM SIGKDD Int. Conf. Knowl. Disc. Data Min., 2019, pp. 761–771.

[KLA09] S. Klamt, U.-U. Haus, and F. Theis, “Hypergraphs and cellular networks,” PLoS Comput. Biol., vol. 5, no. 5, 2009.

[LI17] Li J., Ding G., Zhang X., Wu Q. “Recent Advances in Radio Environment Map: A Survey”, in Machine Learning and Intelligent Communications (MLICOM 2017), vol 226. Springer, Cham. https://doi.org/10.1007/978-3-319-73564-1_25

[MES10] M. Mesbahi and M. Egerstedt, Graph Theoretic Methods in Multiagent Networks. Princeton, NJ, USA: Princeton Univ. Press, 2010, vol. 33.

[MUK16] S. Mukherjee and J. Steenbergen, “Random walks on simplicial complexes and harmonics,” Random Struct. Algorithms, vol. 49, no. 2, pp. 379–405, 2016.

[MUN18] J. R. Munkres, Elements of Algebraic Topology, CRC Press, 2018.

[ORT18] A. Ortega, P. Frossard, J. Kovacevîc, J. M. F. Moura, and P. Vandergheynst, “Graph signal processing: Overview, challenges, and applications,” Proc. of the IEEE, vol. 106, no. 5, pp. 808–828, May 2018.

[PAR17] O. Parzanchevski and R. Rosenthal, “Simplicial complexes: Spectrum, homology and random walks,” Random Struct. Algorithms, vol. 50, no. 2, pp. 225–261, 2017.

[PES14] M. Pesko et al. “Radio Environment Maps: The Survey of Construction Methods.” KSII Trans. Internet Inf. Syst. 8 (2014): 3789-3809.

[POU20] K. Poularakis, J. Llorca, A. M. Tulino, I. Taylor, and L. Tassiulas. Service placement and request routing in MEC networks with storage, computation, and communication constraints. IEEE/ACM Transactions on Networking, 28(3):1047–1060, 2020.

[PUY16] Puy G, Tremblay N, Gribonval R, Vandergheynst P, Random sampling of bandlimited signals on graphs. Applied and Computational Harmonic Analysis 2016.

[ROM17] D. Romero, S. Kim, G. B. Giannakis and R. López-Valcarce, "Learning Power Spectrum Maps From Quantized Power Measurements," in IEEE Transactions on Signal Processing, vol. 65, no. 10, pp. 2547-2560, 15 May15, 2017, doi: 10.1109/TSP.2017.2666775.

[SCH18] M. T. Schaub and S. Segarra, “Flow smoothing and denoising: Graph signal processing in the edge-space,” in Proc. IEEE Global Conf. Signal Inf. Process., Nov. 2018, pp. 735–739.

[SCH18_2] M. T. Schaub, A. R. Benson, P. Horn, G. Lippner, and A. Jadbabaie, “Random walks on simplicial complexes and the normalized Hodge Laplacian,” 2018, arXiv:1807.05044

[SHU13] D.I. Shuman, S. K. Narang, P. Frossard, A. Ortega, and P. Vandergheynst, “The emerging field of signal processing on graphs: Extending high-dimensional data analysis to networks and other irregular domains,” IEEE Signal Process. Mag., vol. 30, no. 3, pp. 83–98, May 2013.

[TSI16] M. Tsitsvero, S. Barbarossa and P. Di Lorenzo, "Signals on Graphs: Uncertainty Principle and Sampling," in IEEE Transactions on Signal Processing, vol. 64, no. 18, pp. 4845-4860, 15 Sept.15, 2016, doi: 10.1109/TSP.2016.2573748

[TUY19] Tuyen X. Tran and Dario Pompili. Adaptive bitrate video caching and processing in mobile-edge computing networks. IEEE Transactions on Mobile Computing, 18(9):1965–1978, September 2019.

[WAN15] X. Wang, P. Liu and Y. Gu, "Local-Set-Based Graph Signal Reconstruction," in IEEE Transactions on Signal Processing, vol. 63, no. 9, pp. 2432-2444, May 1, 2015, doi: 10.1109/TSP.2015.2411217

[WEI13] Z. Wei, Q. Zhang, Z. Feng, W. Li and T. A. Gulliver, "On the construction of Radio Environment Maps for Cognitive Radio Networks," 2013 IEEE Wireless Communications and Networking Conference (WCNC), Shanghai, China, 2013, pp. 4504-4509, doi: 10.1109/WCNC.2013.6555304.

[YANG21] YANG model, O-RAN.WG4.MP.0-v05.00, O-RAN Alliance, 2021

[YIL13] H. B. Yilmaz, T. Tugcu, F. Alagöz and S. Bayhan, "Radio environment map as enabler for practical cognitive radio networks," in IEEE Communications Magazine, vol. 51, no. 12, pp. 162-169, December 2013, doi: 10.1109/MCOM.2013.6685772.

[ZHA20] S. Zhang, Z. Ding, and S. Cui, “Introducing hypergraph signal processing: Theoretical foundation and practical applications,” IEEE Internet of Things Journal, vol. 7, no. 1, pp. 639–660, 2020.